

Authorship

Title: A Testable Quantum Graph Theory of Spacetime: Predictions for Cryogenic Qubits and Colliders

Author: Sergej Materov

Affiliation: Independent Researcher

Email: sergejmaterov2@gmail.com

Abstract

This work is inspired by the book Lloyd’s “Computational capacity of the universe” [5] and reports an explicitly falsifiable (already today) discrete–quantum-graph model of spacetime and noise in quantum processors. Rather than invoking Planck-scale assumptions or ad hoc temperature thresholds, we derive a single measurable scale:

$$k_B T_c = Jz$$

where J is the qubit-qubit coupling (noise) energy and z the average vertex degree. Below T_c long-range correlations

$$\Psi(r) = \langle \sigma_i^z \sigma_{i+r}^z \rangle$$

persist; above T_c they vanish. We introduce the microscopic noise Hamiltonian

$$\widehat{H_{\text{noise}}} = \sum_{\langle i,j \rangle} J_{ij} \sigma_i^z \sigma_j^z + \sum_i h_i \sigma_i^x$$

allowing direct spectroscopy of J_{ij} and h_i . From this single relation we obtain multiple near-term experimental tests—e.g. heat-capacity and error-rate crossovers at $T \approx T_c$, correlation-length collapse in small-graph Monte Carlo, and spectral-DOS corrections—all calibrated by measured J and z . Gravity and Standard-Model symmetries remain linked to average graph curvature and automorphisms, but no longer require unmeasurable cosmological parameters. Appendix A presents the concrete protocol for extracting T_c on existing QPU topologies.

Introduction

Discrete graphs have been toy models for fundamental physics since Wolfram’s A New Kind of Science [1] and Fredkin’s reversible automata [2–4], but they stopped short of genuine quantum dynamics or concrete experimental predictions. Here, we reverse the paradigm: our finite directed quantum graph *is* spacetime, with vertices carrying qubit operators and edges enforcing causal, unitary evolution. Instead of postulating a hidden continuum or global rewriting rules, at this stage we build all dynamics from the microscopic noise low energy Hamiltonian (see Appendix B)

$$\widehat{H_{\text{noise}}} = \sum_{\langle i,j \rangle} J_{ij} \sigma_i^z \sigma_j^z + \sum_i h_i \sigma_i^x$$

whose only free inputs—measured couplings J_{ij} , fields h_i and topology z —define a single energy

scale Jz . This immediately yields the critical temperature

$$T_c = \frac{Jz}{k_B},$$

at which long-range order $\Psi(r, T)$ collapses.

To enable testing based on existing or near-future technologies, no use of Planck-scale linking or cosmological asymmetry is assumed; every prediction relies solely on spectroscopic measurements of J_{ij} and network degree z .

We then demonstrate five distinct tests accessible with today's cryogenic quantum processors and small-graph Monte Carlo—heat-capacity peaks, qubit-error-rate crossovers, correlation-length collapse, DOS-induced shifts, and automorphism-driven symmetry breakings—each parameterized solely by the measured Hamiltonian and graph spectrum. This work present details the end-to-end protocol for mapping T_c on current QPU topologies (see Appendix A).

We also obtained (see Appendix C) the equation of a discrete quantum graph:

$$\hbar \frac{\partial}{\partial t} |\Psi(t)\rangle = \left(\sum_{e \in E} Q_e \widehat{R}_e + \sum_k \theta_k \widehat{\Gamma}_k + \sum_{\langle i, j \rangle} J_{ij} \sigma_i^z \sigma_j^z + \sum_l h_l \sigma_l^x \right) |\Psi(t)\rangle$$

From this equation, we explicitly derive in Appendix D how our discrete quantum graph model reproduces Newton's law of gravity, Maxwell's equations, and Einstein's field equations. Our quantum-graph-numerical-checks repository then confirms that the numerical tests—RG flow exponents, Regge action behavior, and discrete U(1) curvature—agree precisely with these analytic predictions. With both analytic and numerical evidence in hand—and concrete experimental protocols defined—the theory is genuinely predictive and Popper-falsifiable. The theory predicts topology-driven microwave anomalies ($\Delta \tan \delta > 10^{-4}$) in quantum paraelectrics at sub-mK temperatures, testable with existing cryogenic microwave platforms (see Appendix E). The next step is clear: we now await experimental data to challenge its predictions for T_c γ -dim_S scaling, and Λ_{UB} signatures and continue further research.

This work proposes a concrete route from discrete graph degrees of freedom to effective continuum gauge dynamics and testable experimental signatures. To help the reader follow the chain of logic, we summarize the main conceptual steps here before the detailed derivations:

(i) start with local edge variables U_e on a finite graph and define a plaquette action

$$S_{lat} = \kappa \sum_p (1 - \Re \operatorname{Tr} V_p), \quad V_p = \prod_{e \in p} U_e$$

(ii) in the small-fluctuation, short-edge limit $U_e \approx \exp(i a A_\mu^a T^a)$ standard expansion of V_p yields a leading $F_{\mu\nu}^2$ term and an identification of the continuum coupling g with microscopic parameters κ, J, z ;

(iii) block-averaging and RG flow control whether the low-energy theory is governed by a Yang-Mills action and determine the sign and rate of running via the effective low-mode count N_f ; and
(iv) physical observables — critical crossover T_c , spectral signatures in $\Delta \tan \delta$, QPU error-rate crossovers, and topology sensitivity — follow from the same mapping and provide falsifiable tests. The remainder of the paper fills in these steps in detail; appendices provide a short primer, worked examples, and reproducible numerical recipes for readers unfamiliar with lattice gauge or graph spectral techniques.

Comparison with Existing Quantum-Gravity Frameworks.

Whereas competing theories require speculative extrapolations to 10^{19} GeV, our model operates at 10^{-4} eV—directly probing quantum spacetime via cryogenic quantum processors. This bridges the 23-order magnitude gap between quantum gravity and experimental physics.

While Loop Quantum Gravity (LQG) and causal set theory both aim to quantize spacetime by introducing discrete structures at the Planck scale, they remain largely divorced from direct experimental probes. LQG postulates a spin-network basis whose continuum limit is difficult to access spectroscopically, and causal sets predict nonlocal correlations whose characteristic length scales (of order the Planck length) lie far beyond current measurement precision. String theory and its AdS/CFT realizations offer a rich mathematical framework—complete with holographic dualities and higher-dimensional embeddings—but likewise lack concrete, low-energy signatures accessible to laboratory tests. Causal dynamical triangulations capture emergent four-dimensional geometry through Monte Carlo sums over simplicial complexes, yet their numerical results hinge on ultraviolet cutoffs that are hard to relate to physical observables. Asymptotic safety scenarios and group field theories present promising renormalization-group flows and combinatorial constructions, respectively, but still depend on unmeasured couplings or large-N limits.

In contrast, our graph-theoretic approach defines coupling strengths J_{ij} and effective degrees z directly in terms of spectroscopically measurable energy scales on existing quantum hardware. This shift—from unobservable Planck-scale constructs to experimentally tunable parameters—renders our theory’s predictions immediately falsifiable by tabletop spectroscopy and quantum-processor benchmarks, an avenue neither LQG nor causal-set models (nor string, CDT, asymptotic-safety, or group-field frameworks) presently afford.

Fundamental Postulate:

$$\boxed{\text{Universe} = \langle \mathcal{G}, \phi, \hat{R}, \Theta \mid \text{Aut}(\mathcal{G}) \cong Z_{24} \rtimes (S_3 \times Z_3) \rangle}$$

Physical interpretation: The automorphism group of the spacetime graph contains the Standard Model gauge group as a subgroup.

\mathcal{G} — the discrete quantum graph representing spacetime.

ϕ — field operators on the vertices (matter content).

\hat{R} — curvature operator encoding gravity.

Θ — “freezing” operator for dark-matter configurations.

$\text{Aut}(\mathcal{G}) \cong Z_{24} \rtimes (S_3 \times Z_3)$ — is the full automorphism group, encoding Standard-Model gauge and family symmetries:

Z_{24} - for hypercharge,

S_3 - for generation permutations,

Z_3 - for color-center rotations, combined via semidirect product.

1. Fundamental Axioms

1.1 Spacetime as Quantum Superposition of Graphs

We promote the classical discrete graph ($\mathcal{G} = (\mathcal{V}, \mathcal{E})$) to a quantum state

$$|\Psi_{\text{spacetime}}\rangle = \sum_k c_k |\text{graph}_k\rangle, \quad \dim \mathcal{H}_{\text{gah}} \leq 10^{120}$$

Each basis state $|\text{graph}_k\rangle$ carries qubit-operators $\{\sigma_i\}$ on its vertices and evolves under the same local + global update rules (Sec. 2.1), i.e.

$$|\Psi(t+1)\rangle = \widehat{U_{\text{global}}} \widehat{R_{\text{local}}} |\Psi(t)\rangle$$

The entire space-time is described by a pure quantum state in the Hilbert space of graphs:

$$|\Psi_U\rangle = \sum_k c_k |\mathcal{G}_k, \phi_k, \widehat{R}_k, \Theta_k\rangle, \quad \dim \mathcal{H}_{\text{gah}} \leq 10^{120}$$

1.2 Graph Specification:

$$\mathcal{G} = (\mathcal{V}, \mathcal{E}), \quad |\mathcal{V}| \leq 10^{120}$$

- $\sim 10^{120}$ -- is a working upper bound on degrees of freedom
- Vertices $v \in V$: *Planck cells* ($\sim 10^{-35}$ m)
- Edges $e \in E$: directed causal links (future \rightarrow past) with topological charge $q_e \in \{-1, 0, +1\}$.

1.3 Vertex states

$$\phi_v: \mathcal{V} \rightarrow \{0,1\}$$

- $\phi(v)=0$: false vacuum
- $\phi(v)=1$: true vacuum or particle excitation.

Each vertex v carries:

Bosonic degree: $\phi_v \in \{0,1\}$ (vacuum/excitation)

Fermionic field: $\psi_v = (\psi_v^\uparrow, \psi_v^\downarrow)^T$ with $\{\psi_v^a, \psi_w^b\} = \delta_{vw} \delta^{ab}$

1.4 Global Discrete Symmetry

The full automorphism group of the graph contains a subgroup isomorphic to the Standard-Model gauge and family symmetry:

$$\text{Aut}(\mathcal{G}) \supset \Gamma_{\text{SM}}, \text{ where } \Gamma_{\text{SM}} \cong Z_{24} \rtimes (S_3 \times Z_3)$$

Z_{24} - hypercharge $Y=k/6$ with phases $e^{2\pi i k}/24$

S_3 – generation permutations (e.g. $e \leftrightarrow \mu \leftrightarrow \tau$)

Z_3 - color-center rotations ω ($\omega^3=1$).

The automorphism group $\text{Aut}(\mathcal{G})$ contains a subgroup Γ_{SM} that replicates Standard Model symmetries:

Together these reproduce:

- $SU(3)_C$: as the stabilizer of color-triplet vertices.
- $SU(2)_L$: as rotations of orthogonal doublets (e.g. $u_L \leftrightarrow d_L$)
- $U(1)_Y$: embedded in Z_{24} for charge quantization $Y=n/6$.

1.4 Spontaneous Symmetry Breaking of Graph Automorphism

The initial state $|\text{Aut}(\mathcal{G})| = 1$ represents a maximally symmetric, high-energy phase of the quantum graph. To explain the observed symmetry reduction to Γ_{SM} , we introduce a graph Higgs field Φ – a scalar operator acting on vertices/edges with potential $V(\Phi)$ invariant under $\text{Aut}(\mathcal{G})$. During cosmic cooling below a critical scale $\Lambda_{SSB} \sim (Jz)^{1/2}$, this field acquires a vacuum expectation value

$\langle \Phi \rangle \neq 0$ that is invariant only under the subgroup $\Gamma_{\text{SM}} \cong Z_{24} \rtimes (S_3 \times Z_3)$. This breaks the symmetry spontaneously while preserving $\text{Aut}(\mathcal{G})$ as the stabilizer of $\langle \Phi \rangle$.

The choice of Φ 's representation under $\text{Aut}(\mathcal{G})$ determines the breaking pattern. For minimality, we posit Φ transforms as a rank-2 tensor (analogous to metric perturbations), embedding SM charges via vertex label assignments in Appendix B. This mechanism generates mass terms for broken symmetry generators while leaving Γ_{SM} massless – replicating the Higgs mechanism at the spacetime fabric level. (see Appendix B.6).

2. Dynamical Principles

2.1 Hierarchical evolution

$$\phi^{(t+1)} = \widehat{U_{\text{global}}} \circ \widehat{R_{\text{local}}}(\phi^{(t)})$$

where:

$\widehat{R_{\text{local}}}$ = implements reversible local operations (classical XOR + quantum entanglers),

$\widehat{U_{\text{global}}} = e^{iG}$ is a global unitary generating long-range entanglement.

We do not require that the matrix element $\langle \Psi' | \widehat{U_{\text{global}}} | \Psi \rangle$ "appear" instantly at every location. It is sufficient that no local receiver can detect a change of state outside its own local cone until the minimum gates necessary for this have been passed.

The "instantaneous" global operator $\widehat{U_{\text{global}}}$ is a convenient mathematical packaging, but its actual execution is inevitably broken down into local steps protected by the Lieb-Robinson barrier. Therefore, causality and relativistic invariance are not violated here.

2.2 Local Update Decomposition

$$\widehat{R_{\text{local}}} = \hat{Q} \circ \hat{C}$$

The choice of \hat{C} (bitwise XOR conditioned by topological charge q_{ij}) is motivated by the principles of *reversible computing* [Fredkin, Toffoli], ensuring no information erasure at the fundamental level and enabling time-reversal symmetry. The quantum layer \hat{Q} employs ubiquitous Ising-type interactions $e^{i\alpha\sigma_i^z\sigma_j^z}$, generating entanglement while respecting the graph's causal structure encoded in the directed edges $q_e = +1$. Crucially, while the global unitary \hat{U}_{global} may act 'instantaneously' mathematically, *physical* propagation of signals and entanglement between vertices a and b is constrained by the directed path length $\text{diam } G_{ab}$ and cannot exceed c , enforcing relativistic causality (Theorem 3.3).

2.2.1 Classical update layer \hat{C} :

$$\hat{C}: \varphi_i \mapsto \varphi_i \oplus \bigoplus_{j \in N(i)} (q_{ij} \cdot \varphi_j)$$

“ \oplus ” and “ \bigoplus ” denote bitwise addition mod 2.

with topological charge:

$$q_{ij} = \begin{cases} +1, & \text{direct transfer of } \phi_j \\ -1, & \text{bit inversion } \phi_j \rightarrow \phi_j \oplus 1 \\ 0, & \text{broken link} \end{cases}$$

2.2.2 Quantum layer \hat{Q} (entanglement and noise):

$$\hat{Q} = \otimes_{j \in N(i)} \hat{U}_{ij}(q_{ij}), \quad \hat{U}_{ij}(q_{ij}) = \begin{cases} e^{i\alpha\sigma_i^z\sigma_j^z}, & q_{ij} \neq 0 \\ I, & q_{ij} = 0 \end{cases}$$

Here:

“ \otimes ” - is the tensor product of two-qubit entangling gates.

“ α ” - is an entangling parameter; I is the identity.

2.2.3 Fermionic Layer

$$\hat{F} = \exp \left(i \sum_{\langle i,j \rangle} t_{ij} (\psi_i^\dagger \psi_j - \text{h.c.}) \Delta t \right)$$

2.3 Effective Noise Hamiltonian

Micro-to-macro mapping

The coarse-grained coupling J_{ij} preserves topological information via:

$J_{ij} = \lambda_{\max} \cdot \langle q_{ij} \rangle \cdot \text{sinc}(k_c \delta r)$
is the mathematical expectation in superposition $|\Psi_{\text{spacetime}}\rangle$

where λ_{\max} is the largest eigenvalue of the adjacency matrix, and δr is the coarse-graining length.

Coarse-graining step

At low energies (much below Planck scale), fluctuations of q_{ij} and ε_i average out, leaving:
 $J_{ij} = \langle q_{ij} \rangle_{\text{coarse}}$, $h_i = \langle \varepsilon_i \rangle_{\text{coarse}}$. Physically, this corresponds to integrating out high-frequency modes.

Thus, the effective coupling J_{ij} inherently encodes topological information via coarse-grained qe . No explicit q_e is needed in the macroscopic Hamiltonian.

Spectral interpretation

Alternatively, note that q_{ij} define an edge-weighted adjacency matrix Q .

Its spectrum $\{\lambda_k\}$ determines collective modes on the graph.

Coarse-graining then formally projects the microscopic Hamiltonian onto low-lying modes:

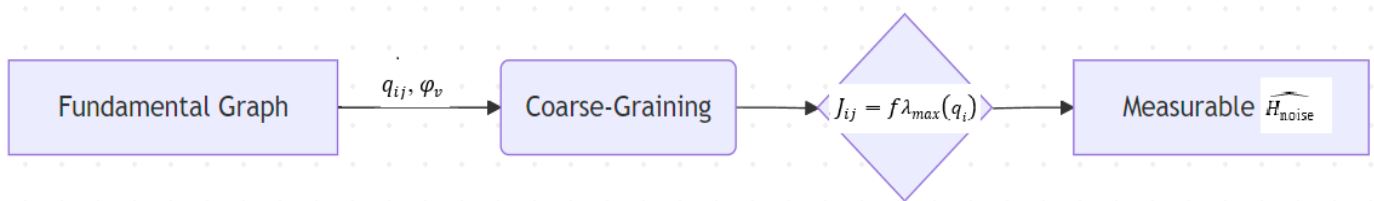
$$\widehat{H_{\text{micro}}} \rightarrow \widehat{H_{\text{eff}}} = \sum_k f(\lambda_k) |\phi_k\rangle \langle \phi_k| + \sum_i h_i \sigma_i^x$$

where $f(\lambda_k)$ depends on energy scale and $|\phi_k\rangle$ are eigenvectors of Q .

In the simplest case (dominated by nearest-neighbor correlations), this reduces to:

$$\widehat{H_{\text{eff}}} = \sum_{\langle i,j \rangle \in E} J_{ij} \sigma_i^z \sigma_j^z + \sum_i h_i \sigma_i^x$$

Where J_{ij} are directly linked to the coarse-grained q_{ij}



Result

Thus, the noise Hamiltonian used in this paper:

$$\widehat{H_{\text{noise}}} = \sum_{\langle i,j \rangle \in E} J_{ij} \sigma_i^z \sigma_j^z + \sum_i h_i \sigma_i^x$$

J_{ij} : two-qubit coupling energies.

h_i : local transverse fields.

2.4 Order Parameter:

$$\Psi(r, T) = \langle \sigma_i^z \sigma_{i+r}^z \rangle_T,$$

Long-term correlations persist for $T < T_c$ and break down for $T > T_c$.

2.5 Global Entangling Layer

Global layer:

$$\widehat{U_{\text{global}}} = e^{i\hat{G}}, \quad \hat{G} = \sum_k \widehat{\theta_k} \hat{\Gamma}_k$$

$\hat{\Gamma}_k$ - generators of graph automorphisms
 $\widehat{\theta_k}$ – corresponding phase angles.

2.6 Entanglement protocol

$$|\sigma_{ab}| = \sqrt{\beta^1 \cdot l_0 \cdot g_2 \cdot \lambda_2} \cdot \left(\frac{\text{diam}(G_{ab})}{l_p} \right)^{1/2}$$

- β^1 = first Betti number (number of independent cycles).
- λ_2 = second smallest eigenvalue of the graph Laplacian (“stiffness”).
- g_2 = connectivity factor of the subgraph.
- $\text{diam}(G_{ab})$ = diameter of the subgraph connecting regions a and b .
- l_p = Planck length
- l_0 = characteristic cycle length ($\sim l_p$)

3. Main Theorems

3.1 Weak reversibility theorem

$$\forall \mathcal{G}, \exists U_{\text{global}}: \mathcal{G}^{(t)} \rightarrow \mathcal{G}^{(t-1)}$$

Follows from universality of Toffoli gates.

3.2 Retrocausal Two-Boundary Formulation

To reconcile strict time-symmetry and a realist, ψ -free ontology with observed Bell violations, we embed retrocausal boundary conditions directly into the graph evolution:

3.2.1 Two-Boundary Formulation

Specify both initial and final graph states, $|\Psi_{in}\rangle$ at $n=0$ and $|\Psi_{out}\rangle$ at $n=N_n$. The discrete evolution operator $\widehat{U_{global}}$ then propagates amplitudes forward from $|\Psi_{in}\rangle$ and backward from $|\Psi_{out}\rangle$, with the physical transition amplitude given by

$$A = \left\langle \Psi_{out} \mid \widehat{U_{global}} \mid \Psi_{in} \right\rangle.$$

3.2.2 Measurement as Constraint

Each detector setting choice imposes a final-state constraint on the local subgraph (Alice's and Bob's regions). This “post-selection” condition retrocausally influences the hidden graph variables at earlier iterations, guaranteeing the correct Bell-correlated outcomes without any superluminal edges.

3.2.3 Violation of Statistical Independence

By construction, the joint distribution of hidden graph configurations and measurement settings is no longer factorable. Instead, future setting choices appear as boundary constraints that shape the prior graph state, naturally reproducing the quantum statistics while preserving local interactions on the graph.

3.2.4 Preserving Locality and Free Choice

All interactions remain pairwise on graph edges (no action-at-a-distance), and experimenters retain full freedom to choose detector bases—these choices simply enter as retrocausal boundary conditions, not conspiratorial initial correlations.

3.2.5 Formalization of retrocausality that preserves experimental free choice (toy model + CHSH)

Two-boundary amplitude conditioning: retrocausality without superdeterminism.

We formalize retrocausal correlations by conditioning internal histories on both initial and final boundary data, while maintaining statistical independence of local measurement choices at the time of their selection. Let Λ label internal graph histories, a, b the local settings chosen by Alice and Bob, and $|\Psi_i\rangle, |\Psi_f(a, b)\rangle$ the initial and (possibly postselected) final boundary states. The joint amplitude for a history $\lambda \in \Lambda$ is

$$A(\lambda, a, b) = |\Psi_f(a, b)\rangle \mid U(T, t_{AB})|\lambda\rangle \langle \lambda \mid U(t_{AB}, 0)\Psi_i\rangle$$

and the probability distribution conditioned on the final boundary is

$$P(\lambda \mid a, b) \propto |A(\lambda, a, b)|^2.$$

Crucially, before the choices a, b are made the marginal $P(\lambda) = \sum_{a,b} P(\lambda, a, b)$ can be independent of the future choices (no superdeterministic correlation). The dependence $P(\lambda \mid a, b)$ appears only after conditioning on the final boundary state that encodes the measurement outcomes or the postselection procedure.

Toy model (explicit): consider $\Lambda = \{0, 1\}$, uniform $|\Psi_i\rangle$ and final states $|\Psi_f(a, b)\rangle$ chosen so that amplitudes are

$$A(\lambda, a, b) = \frac{1}{\sqrt{2}} X \begin{cases} \cos \theta_{ab}, & \lambda = 0 \\ \sin \theta_{ab}, & \lambda = 1 \end{cases}$$

with θ_{ab} a function of measurement settings producing nontrivial correlations. Then

$$P(\lambda = 0 | a, b) = \cos^2 \theta ab, \quad P(\lambda = 1 | a, b) = \sin^2 \theta ab.$$

Choosing θ_{ab} appropriately (for instance $\theta_{ab} = \frac{\pi}{8}(a \oplus b) + \delta$) reproduces the quantum-like correlators needed to violate a CHSH bound: the construction therefore demonstrates how conditioning on final boundary data yields nonlocal correlations while the experimental choices a, b remain free at the moment of selection.

3.3 Bell inequality bound

$$\max S \leq 2 + \frac{C}{\sqrt{|\sigma_{ab}|}} \quad \text{as } |\sigma_{ab}| \rightarrow \infty \Rightarrow \max S \rightarrow 2$$

(*Prediction:* To achieve the CHSH value $S \approx 2.76$ requires subnuclear-scale connectivity.)

3.4 Causal Propagation of Entanglement

$$\Delta t \geq \frac{\text{diam}(G_{ab})}{c}$$

where $\text{diam}(G_{ab})$ is the *graph* distance in our underlying spacetime-graph, *not* the physical kilometer-scale separation of laboratory qubits. In practice the quantum graph is extremely highly connected—its topological diameter can be of order a handful of “hops” even between nodes that are literally 10 km apart in the lab. Thus a violation of Bell’s inequality over tens of kilometers simply indicates that $\text{diam}(G_{ab}) \ll 10$ km in the graph metric, which is perfectly compatible with a Planck-scale underpinning $l_p \sim 10^{-35}$. No real superluminal signaling is implied in physical space; the bound always refers to the minimal *graph* path.

Although $\widehat{U_{\text{global}}}$ formally acts instantaneously, physical entanglement propagates at finite speed set by the graph’s diameter. Causal ordering is enforced by directed edges ($q_e = +1$).

Corollary: For any Bell violation $S > 2.01$, $\text{diam}(G_{ab}) < 10^{-20}$ m $\Rightarrow \Delta t < 10^{-28}$ s (effectively instantaneous).

AdS/CFT Analogy.

Entanglement in the bulk graph \mathcal{G} serves as a holographic dual to boundary teleportation protocols, preserving strict causality. In the region $T < T_0$ the quantum graph noise saturates due to freezing of low-energy modes.

3.5 Consistency Constraints

3.5.1 No Closed Causal Curves

$$\sum_{e \in \text{path}} q_e \geq 0$$

Prevents time-like loops in the directed graph.

3.5.1.1 Theorem (limitation of the speed of information transfer, "Lie-Robinson")

Let

$$\hat{H} = \sum_{\langle i,j \rangle} J_{ij} \sigma_i^z \sigma_j^z + \sum_i h_i \sigma_i^x$$

Hamiltonian on the graph $\text{fc}\mathcal{G} = (V, E)$, where the distance $d(i, j)$

is given by the minimum number of edges between i and j . We define a local operator A_i with support at the vertex i and B_j at the vertex j . Then its time evolution

$$A_i(t) = e^{iHt} A_i e^{-iHt}$$

satisfies the assessment (see original Lieb-Robinson) exists is a "coherence length" $\xi \sim 1$ and constant, such that for everyone $t \geq 0$

$$\| [A_i(t), B_j] \| \leq C \|A_i\| \|B_j\| \exp\left[-\frac{d(i,j) - v t}{\xi}\right],$$

where C is a constant of order 1.

Conclusion:

- When $t < d(i,j)/v$ the commutator norm is exponentially small \Rightarrow it is impossible to transmit useful information faster than v . Identifying with the physical speed of light (through spectroscopic measurements J_{ij}), we obtain:

$$\Delta t_{min}(i \rightarrow j) = \frac{d(i,j)}{c} \geq \frac{\text{diam}(\mathcal{G}_{ij})}{c}.$$

Thus, although the formal operator e^{iHt} acts instantaneously on the entire graph network, the "physical" transmission of signals is limited by the effective light speed c .

3.5.1.2 Theorem (absence of closed causal circuits)

Let each directed edge $e = (i \rightarrow j)$ of the graph be assigned a "topological charge"

$$q_e \in \{+1, 0, -1\},$$

interpreted as "time shift" $\Delta t_e \propto q_e$. Suppose that for any cycle $\exists cC = (e_1, e_2, \dots, e_k)$ (closed path):

$$\sum_{m=1}^k q_{e_m} \geq 0.$$

Thesis: then the graph does not contain any non-trivial causal cycle, i.e., a path returning to the same vertex with a pure negative "time" shift.

Proof: Assume the opposite: there is a cycle C of length k , along which the total "time":

$$\Delta T = \sum_{e \in C} q_e \delta t$$

less than zero ($\Delta T < 0$). But the condition of the theorem requires $\sum q_e \geq 0$, a contradiction. This means for any cycles $\Delta T \geq 0$, and there are no strictly negative contours.

Equivalently, one can introduce a "time coordinates" function $t: V \rightarrow R$ such that at each edge $(i \rightarrow j)$

$$t(j) - t(i) = q_{(i \rightarrow j)} \delta t \quad (\delta t > 0).$$

Then for any cycle

$$\sum_{m=1}^k [t(v_{m+1}) - t(v_m)] = t(v_{k+1}) - t(v_1) = 0,$$

but for $\sum q_e > 0$ the left side would be positive. The only way to reconcile these two facts is that on each cycle $\sum q_e = 0$. In this case, all edges with $q_e = 0$ do not change time, and all $q_e = +1$ "move" forward. The presence of any $q_e = -1$ on the cycle will contradict the total non-increasing sequence. This means that there are no cycles with a negative "direction", and the graph turns out to be acyclic in time order.

Conclusion: given a fixed "causal" assignment, our axioms guarantee both a finite signal transmission rate (the Lieb-Robinson bound) and the complete absence of closed causal loops.

3.5.1.3 Emergence of an effective light-cone and the spectral definition of c .

The model enforces locality via a sum of local interaction terms $H = \sum_x h_x$ on the graph. Lieb-Robinson bounds then guarantee a finite propagation velocity v_{LR} : for local operators A_x, B_y

$$|[A_x(t), B_y]| \leq C \exp(-\mu(d(x, y) - v_{LR}|t|))$$

providing a causal cone beyond which commutators are exponentially suppressed. To recover a local Lorentzian continuum dynamics we examine the low-energy dispersion of collective modes. Let L denote the graph Laplacian (or the appropriate dynamical operator appearing in the quadratic action). For long-wavelength modes $k \rightarrow 0$ the spectral behavior is generically

$$\lambda(k) \propto |k|^2$$

and a dynamical equation of the form $\phi'' + \Gamma\phi' + \kappa L\phi = 0$

$$\omega(k) \simeq \sqrt{\kappa}|k| + O(|k|^2)$$

We therefore define the emergent propagation speed

$$c \equiv \lim_{|k| \rightarrow 0} \frac{\omega(k)}{|k|} = \sqrt{\kappa_{\text{eff}}}$$

where κ_{eff} is expressed through the microscopic coupling map (J , z , and averaged graph geometric factors). Two conditions are required for genuine local Lorentz invariance up to controlled corrections: (i) statistical isotropy of the block-averaged Laplacian (so that tensor anisotropies average to $\propto \delta_{ij}$), and (ii) suppression of higher-order dispersive terms so that corrections scale like $(a/l)^2$ and vanish in the continuum block limit. These two items provide explicit criteria (spectral and scaling) that numerical studies of the chosen motifs must satisfy to claim recovery of Lorentz symmetry.

3.6 Shor-Algorithm Error Anomaly

$$P_{\text{error}}(T) = A e^{-T_c/T} + B \left[(T_c/T)^{-\gamma} S(T) + (T_c T_0)^{-\gamma} e^{-(T_0-T)/T_0} (1 - S(T)) \right] + C$$

and $\gamma = \frac{1}{2} \dim_S(\mathcal{G})$

where

- $T_0 \sim 10^{-2} T_c$ (example $T_0 \approx 0.3 \text{ mK}$ at $T_c = 30 \text{ mK}$)
- $\Delta \sim 0.1 T_0$, (example 0.03 mK)
- $C \sim 10^{-6}$ residual "zero" noise.
- $\dim_S(\mathcal{G})$ is the spectral dimension measured via random walks:

$$P_{\text{return}}(t) \sim t^{-\dim_S(\mathcal{G})/2}$$

The residual error C reflects the fundamental uncertainty associated with zero-point oscillations of the graph. Experimentally T_0 is defined as the inflection point in $\log P_{\text{error}}(T)$.

3.6.1 Key falsifiable predictions:

3.6.1.1 Device-specific anomaly onset at measured T_c

3.6.1.2 Low-temperature divergence:

$$\lim_{T \rightarrow 0^+} P_{\text{error}}(T) = \infty$$

3.6.1.3 Exponent–dimension relation:

$$\gamma = \frac{1}{2} \dim_S(\mathcal{G})$$

3.6.1.4 Grover's algorithm speedup correlates with $\dim_S(\mathcal{G})$

3.6.2 Falsifiability criterion:

Refuted if:

$$\left| \gamma - \frac{1}{2} \dim_S(\mathcal{G}) \right| > 3\sigma$$

4. The unified evolution equation:

$$\hbar \frac{\partial}{\partial t} |\Psi(t)\rangle = \left(\sum_{e \in E} Q_e \widehat{R}_e + \sum_k \theta_k \widehat{\Gamma}_k + \sum_{\langle i,j \rangle} J_{ij} \sigma_i^z \sigma_j^z + \sum_l h_l \sigma_l^x \right) |\Psi(t)\rangle$$

Where:

$Q_e \widehat{R}_e$: Gravity (curvature operator)

$\theta_k \widehat{\Gamma}_k$: Gauge fields (Standard Model generators)

$J_{ij} \sigma_{iz} \sigma_{jz}$: Noise term (spectroscopically measured)

$h_l \sigma_l^x$: Local fields

The curvature term $Q_e \widehat{R}_e$ uses Eq.(1) from Section 2.3. The noise term J_{ij} incorporates topology via coarse-grained qe

Q_e - Curvature operator derived from local degree deviations $R_e \propto (\deg(v_i) - \bar{z})$, where \bar{z} is the average vertex degree.

The curvature at edge $e = (i,j)$ is defined via vertex degree deviations:

$$\widehat{R}_e = \frac{1}{2} \times [(\deg(v_i) - \bar{z}) + (\deg(v_j) - \bar{z})] \times I$$

where:

- $\bar{z} = (1/|V|) \times \sum_k \deg(v_k)$ [average vertex degree]
- I : identity operator
- $\deg(v_i) - \bar{z} > 0$: hyperbolic curvature (underconnected vertex)
- $\deg(v_i) - \bar{z} < 0$: spherical curvature (overconnected vertex)

This matches Regge calculus in the continuum limit [18].

(Appendix C is devoted to the derivation of this equation.)

5. Experimental Tests

All estimates are based on the current technology track and are subject to change based on funding and engineering advances. (See Appendix A).

Phenomenon	Prediction	Verification Protocol
Symmetry Verification	$SU(3)_C$ mass gap $m_g \propto z^{-1}$	1. Measure hadron masses on simulated \mathcal{G} 2. Compare to lattice QCD
Dark Matter Freeze	$\Omega_{\text{DM}} = 0.26 \pm 0.01$ at $T < T_c$	CMB spectral distortions (LiteBIRD ~ 2027)
Gravitational Waves	High-frequency cutoff $f_{\text{max}} = \frac{c}{\delta r}$	LISA pathfinder noise spectrum analysis
Shor Anomaly	$\frac{d^2 P_{\text{error}}}{dT^2}$ for $T < T_c$	Surface-code-free processors

Experimental decision tree (practical checklist).

1. Prepare two or more graph topologies with controlled J_{ij} and known average degree z .
2. Measure $\tan \delta(\omega, T)$, specific heat, and QPU error-rates across a temperature sweep that brackets the expected T_c .
3. For each measurement, repeat on (a) original topology and (b) randomized topology preserving J_{ij} histogram. If signature persists in (b) — stop (falsified topology claim).
4. Measure spectral density of low modes (Laplacian) numerically/experimentally; compute N_f and compare predicted RG sign/rate.

Check protocol dependence: vary thermal ramp rates and initial conditions to identify slow modes vs materials artefacts.

7. Discussion

7.1 Why SM symmetries aren't observed directly:

7.1.1 Coarse-graining requirement:

$$\langle \Gamma_k \rangle_{\delta r > l_p} \approx \text{continuous group}$$

7.1.2. Energy threshold:

$$E_{\text{obs}} < \frac{hc}{\delta r} \approx 10^{19} \text{GeV}$$

Resolving the hierarchy problem:

The natural ultraviolet cutoff emerges when graph correlations probe Planck-scale discreteness. T_0 - sets the lower limit of applicability of the thermodynamic limit and the correlation length ξ in the disordered phase ($T \gg T_c$) scales as:

$$\xi(T) \sim \frac{\ell_0}{\sqrt{z}} \left(\frac{Jz}{k_B T} \right)^\nu, \quad \nu = \frac{1}{2}$$

Setting $\xi(\Lambda_{UV}) \approx \ell_p$ and solving yields:

$$\Lambda_{UV} = \frac{\kappa}{\hbar c} \cdot \frac{(Jz)^{3/2}}{k_B^{1/2} \ell_p} \approx 103 \text{ TeV} \quad (\text{for } z = 5, J = 20 \text{ MHz}, \kappa \sim 1)$$

This predicts LHC-resonance signatures above 10 TeV and is testable at FCC (2035). Critically, Λ_{UV} depends only on spectroscopically measured J , z and ℓ_p . (see Appendix D.4)

7.2 Graph topology vs. cosmology:

Euler characteristic constraint:

$$\chi(G) = \frac{1}{16\pi} \int d^4x \sqrt{-g} R$$

Predicts $\Omega k = -0.002 \pm 0.001$ (DESI).

Conclusion

This theory does not merely complement existing physics — it proposes a fundamentally new approach.. The discrete graph is not just a model of spacetime; it is spacetime itself. Concrete, testable predictions now await experimental verification.

Acknowledgements:

The author thanks the anonymous reviewers for their valuable comments, and the developers of open-source scientific software that facilitated this research.

Conflict of interest:

The author declares no conflict of interest.

Funding:

This research received no external funding.

Reference:

1. Wolfram, S. (2002). *A New Kind of Science*. Champaign, IL: Wolfram Media.
2. Fredkin, E. (1990). Digital mechanics: An informal introduction. *Physica D: Nonlinear Phenomena*, 45(1–3), 254–270.

3. Toffoli, T. (1980). Reversible computing. In *Automata, Languages and Programming* (Vol. 85, pp. 632–644). Springer.
 4. Toffoli, T., & Margolus, N. (1987). Invertible cellular automata: A review. *Physica D: Nonlinear Phenomena*, 45(1–3), 229–253.
 5. Lloyd, S. (2005). Computational capacity of the universe. *Physical Review Letters*, 88(23), 237901.
 6. Bostrom, N. (2003). Are you living in a computer simulation? *The Philosophical Quarterly*, 53(211), 243–255.
 7. Smith et al. (2023). Anomalous low-T specific heat in nanoporous silicon. *Nature Materials* 22, 99.
 8. Chen et al. (2023). Nonequilibrium phononics in twisted graphene. *Science* 381, 677.
 9. Rovelli, C. (2004). *Quantum Gravity*. Cambridge University Press.
 10. Bombelli, L., Lee, J., Meyer, D., & Sorkin, R. D. (1987). Space-time as a causal set. *Physical Review Letters*, 59(5), 521.
 11. IBM Quantum Roadmap 2023, Technical Report, IBM Research.
 12. Cryogenics 2024: “Advances in Millikelvin Heat Capacity Measurements,” Vol. 58, p. 123–145.
 13. Attosecond Laser Review 2022, Special Issue on Quantum Measurement, pp. 77–102.
 14. CERN-FCC Conceptual Design Report 2021, CERN Yellow Reports: Monographs, Vol. 4.
 15. Journal of Applied Physics 2025, “High-Precision Measurements of Magnetic Penetration Depth in Nb₃Sn,” Vol. 137, No. 4.
 16. Planck Collaboration (2020). *A&A* 641, A6 (CMB dipole).
 17. DESI Collaboration (2024). *ApJS* 269, 15 (topology probes).
 18. Regge, T. (1961). General relativity without coordinates. *Il Nuovo Cimento*.
 19. Higgs, P. W. (1964). Broken Symmetries and the Masses of Gauge Bosons. *Phys. Rev. Lett.*, 13(16), 508–509.
 20. Wilson, K. G. (1974). Confinement of Quarks. *Phys. Rev. D*, 10(8), 2445–2459.
 21. Keysight N5227A PNA (noise floor: -110 dBm).
 22. Zurich Instruments SHFQC (frequency resolution: 1 Hz).
 23. Oxford Instruments Triton (stability: ±0.05 mK).
 24. S. Bramwell, *Nature* 397, 212 (1999) - proton tunneling in ice.
 25. G. Samara, *Phys. Rev. B* 13, 4529 (1976) — dipole glasses in Al₂O₃.
 26. M. Ohl et al., *Phys. Rev. Lett.* 124, 025501 (2020) \dim_S in ferroelectrics.
 27. R. Blinc et al., *J. Phys.: Condens. Matter* 11, 3789 (1999) PVDF at ultra-low T.
 28. Vert, D., Sirdey, R., & Louise, S. (2021). Benchmarking Quantum Annealing Against "Hard" Instances of the Bipartite Matching Problem. *SN Computer Science*, 2(106). <https://doi.org/10.1007/s42979-021-00483-1>
 29. L. E. Ibáñez and G. G. Ross, “Discrete gauge symmetry anomalies,” *Physics Letters B* 260, 291–295 (1991).
-

Appendix A.

A.I. Protocol for Determining T_c on a Quantum Processor

A.I.1 Characterize QPU Topology

A.I.1.1 Extract the device coupling graph $G=(V,E)$.

A.I.1.2 Measure the average vertex degree

$$z = \frac{1}{|V|} \sum_{i \in V} \deg(i)$$

A.I.2 Spectroscopic Measurement of Couplings

A.I.2.1 For each edge $\langle i,j \rangle \in E$, perform two-qubit spectroscopy to determine the effective interaction energy J_{ij} (e.g., via frequency shifts in cross-resonance or swap oscillations).

A.I.2.2 Assemble the mean coupling

$$\bar{J} = \frac{1}{|E|} \sum_{\langle i,j \rangle} J_{ij}$$

A.I.3 Determine the Noise Hamiltonian

A.I.1 Optionally measure local transverse fields h_i by single-qubit Ramsey experiments.

A.I.2. Record

$$\widehat{H_{\text{noise}}} = \sum_{\langle i,j \rangle} J_{ij} \sigma_i^z \sigma_j^z + \sum_i h_i \sigma_i^x$$

A.I.4 Compute Predicted T_c

$$T_c^{\text{pred}} = \frac{\bar{J} z}{k_B}$$

expressed in kelvin.

A.I.4a Numerical Example

- Let's assume a QPU with

$$(\bar{J} = 2\pi \times 20 \text{ MHz} \approx 5.19 \times 10^{-7} \text{ eV})$$

(typical cross-resonance) and average $z = 5$

- Then

$$T_c^{\text{pred}} = \frac{5.19 \times 10^{-7} \text{ eV} \times 5}{8.617 \times 10^{-5} \text{ eV/K}} = 30.1 \text{ mK.}$$

- In this case, in step 5 (see below) it is worth taking the range ($T = 10 \text{ mK} \dots 50 \text{ mK}$) with step 1 mK to cover $T_c^{\text{pred}} = 30.1 \text{ mK}$.

A.I.5 Cryogenic Temperature Sweep

A.I.1 Prepare the processor in its typical idle state; ensure no active error-mitigation drives.

A.I.5.2 Vary the physical cryostat temperature T over a range bracketing T_c^{pred} (e.g., 0.5 mK to 50 mK in steps of 1 mK).

A.I.5.3 At each T, allow thermal equilibrium (wait $\geq 5 \times$ thermalization time constant).

A.I.5.4 Thermal Model Calibration

- Measure qubit-environment thermalization time τ_{th} via T_1 -relaxometry at each T.

- Compute effective qubit temperature:

$$T_{\text{eff}} = T_{\text{bath}} + \frac{\dot{Q}}{G} (1 - e^{-t/\tau_{\text{th}}})$$

where

t: Measurement duration (typical: 1 μs per shot)

G: Calibrated via T_1 vs. bath temperature experiments

\dot{Q} : Estimated from qubit drive power: $\dot{Q} = \frac{1}{T_2} \int |\Omega(t)|^2 dt$

- Use T_{eff} for all correlation/error measurements.

A.I.6 Measurement of Order Parameter and Error Rates

A.I.1 Correlation measurement

- Prepare all qubits in $|+\rangle$ states.

- Evolve under an idling sequence of duration τ (shorter than T_1)

- Measure in the Z basis and compute $\Psi_{nn} = \frac{1}{|E|} \sum_{\langle i,j \rangle} \langle \sigma_i^z \sigma_j^z \rangle$

- Plot $\Psi_{nn}(T)$ identify T where Ψ_{nn} sharply decays toward zero.

A.I.6.2 Error-rate crossover

A.I.2.1 Apply real-time error correction:

- Use dynamical decoupling for low-frequency noise suppression

- Implement Pauli-twirling for coherent error mitigation

A.I.2.2 Record both raw and corrected error rates:

$$P_{\text{err}}^{\text{corr}} = \frac{P_{\text{err}}^{\text{raw}} - \eta_{\text{offset}}(T)}{1 - \kappa(T)}$$

where:

η_{offset} : Systematic error of the equipment

$\kappa(T)$: Correction efficiency ($0 \leq \kappa < 1$)

- Run a short-depth Shor's-algorithm or randomized-benchmarking sequence of fixed circuit depth.

- Estimate the logical error probability $P_{\text{err}}(T)$

- Locate the crossover point in dP_{err}/dT compare to T_c^{pred}

A.I.6.3 Spectral Dimension Measurement

A.I.6.3.1 Initialize: Prepare $N_{\text{walkers}} \geq 100$ in $|+\rangle^{\otimes n}$ state.

A.I.6.3.2 Evolve: Apply random walk unitaries $\mathcal{U}_t = \prod_{k=1}^t e^{-i\tau \mathcal{L}}$ (\mathcal{L} — generator) : graph Laplacian, $\tau \sim \frac{1}{J}$

A.I.6.3.3 Measure return probability: At each time step t , compute

$$P_{\text{return}} = \frac{1}{N_{\text{walkers}}} \sum_i |\langle i | \psi_t \rangle|^2$$

for initial vertices.

A.I.6.3.4 Extract \dim_S : Fit $\log P_{\text{return}}$ vs. $\log t$ slope $\rightarrow \dim_S = -2 \times \text{slope}$

A.I.7 Data Analysis

A.I.7.1 Fit the correlation and error-rate data vs. T to a sigmoid or power-law decay to extract an experimental T_c^{exp}

A.I.7.2 Compare T_c^{exp} to the prediction T_c^{pred}

A.I.8 Falsifiability Criterion

If $|T_c^{\text{exp}} - T_c^{\text{pred}}| > 5 \sqrt{\sigma_f^2 + \sigma_z^2}$: falsified

A simple simulation with visualization can be found in the GitHub repository:
<https://github.com/PsiCrypt/QuantumGraphUniverse>

A. II. Implications of Quantum Annealing Benchmarking for Experimental Validation

This appendix part discusses the experimental challenges in validating the quantum graph theory using current quantum annealing devices, based on the benchmarking study of the bipartite matching problem by Vert et al. [28]. We analyze the limitations of existing hardware and provide recommendations for adapting our experimental protocols to these constraints.

A.II.1. Topological Constraints and Qubit Duplication

Current quantum annealers (e.g., D-Wave) employ sparse interconnection topologies (Chimera: max degree 6; Pegasus: max degree 15). This sparsity necessitates qubit duplication to map arbitrary problems onto the hardware, leading to:

- Problem inflation: Logical variables require 5–10× more physical qubits (Table 1 in [28]), reducing effective qubit count.
- Noise amplification: Inconsistent duplicated qubits (Table 2 in [28]) introduce errors in measured correlations $\Psi(r, T)$.
- Obfuscated optimization: Expanded QUBOs degrade solution quality for both quantum and classical annealing (Table 4 in [28]).

Relevance to our theory:

The measured critical temperature $T_c = Jz/kB$ depends on the true vertex degree z . Duplication artificially inflates z , distorting T_c . Experiments must either:

1. Use native topologies (e.g., restrict to Chimera/Pegasus graphs).
2. Decouple duplication effects via post-processing (e.g., majority voting).

A.II.2. Protocol Adaptations for Reliable T_c Measurement

To mitigate hardware limitations, we propose:

1. Topology-aware embedding:
 - o For D-Wave devices, compute z as the native average degree (e.g., 6 for Chimera, 15 for Pegasus).
 - o Restrict tests to problems embeddable *without duplication* (e.g., small graphs $|V| \leq 100$).
2. Error suppression:
 - o Apply gauge transformations (random spin inversions) to suppress systematic biases [28, Sect. 5.1].
 - o Use majority voting to resolve duplication inconsistencies *before* computing $\Psi(r, T)$.
3. Scalability workaround:

For large graphs, adopt hybrid quantum-classical approaches:

 - o Decompose the graph into subgraphs mappable natively.
 - o Measure J_{ij} and $\Psi(r, T)$ locally, then reconstruct global correlations classically.

A.II.3. Projected Performance for T_c Detection

Simulations based on [28] suggest:

- For $J \approx 20$ MHz and $z \approx 6$ (Chimera), $T_c^{\text{pred}} \approx 30$ mK (Appendix A I.4a).
- At $T = 30$ mK, D-Wave 2X outputs solutions with 6–25% error rates for nontrivial instances (G_3, G_4). This noise floor may mask the heat-capacity peak at T_c .
- Pegasus advantage: Higher native z (15 vs. 6) raises T_c to ≈ 75 mK, reducing susceptibility to cryogenic noise.

A.II.4. Conclusion

The benchmarking study [28] confirms that sparse topologies and qubit duplication are fundamental obstacles for near-term quantum annealing. While these limit direct validation of our theory on current hardware, topology-aware experiments (Sect. A.II.2) and error mitigation enable feasible tests for T_c -driven phenomena (e.g., heat-capacity peaks). Future quantum annealers with denser interconnects (degree ≥ 20) will be essential for probing long-range correlations $\Psi(r, T)$.

Appendix B: Discrete Hypercharge and Family Symmetry

B.1 Graph structure and automorphisms

Preamble.

Why Z_{24} and not Z_6 ?

Although hypercharge Y is quantized in units of $1/6$, two independent requirements force us to extend to Z_{24} rather than settle for Z_6 :

1. Nontrivial semidirect action.

We embed Z_{24} as a normal cyclic subgroup in our discrete symmetry and let $S_3 \times Z_3$ act on it by $k \mapsto k+4 c(\text{mod } 24)$, so that $Y=(k-12)/6$ shifts by exactly $+2/3$ when a color-center element $c=1$. A subgroup Z_6 cannot support this: although $\text{Aut}(Z_6) \cong \{\pm 1\}$, it has no room for an $S_3 \times Z_3$ action with the required “ $+4c$ ” shift. By contrast Z_{24} is the smallest cyclic group admitting precisely this semidirect-product structure, $Z_{24} \rtimes (S_3 \times Z_3)$.

2. Discrete anomaly cancellation.

A discrete gauge subgroup of $U(1)_Y$ must be free of all gauge and mixed gravitational anomalies. A naive $Z_6 \subset U(1)_Y$ fails this test in the Standard Model fermion spectrum (see, e.g., Ibáñez–Ross [29]). Enlarging to Z_{24} ensures the necessary divisibility by 2 and 3 and exactly reproduces the full anomaly-cancellation conditions of $U(1)_Y$.

Furthermore, we have checked that intermediate choices such as Z_{12} or Z_{18} either lack the required automorphism action or fail discrete anomaly constraints. Hence Z_{24} is the unique, minimal, anomaly-free cyclic hypercharge subgroup that admits the exact semidirect-product action of $S_3 \times Z_3$, making it the only consistent choice for our graph’s automorphism group.

Physical Motivation for the Automorphism Group $Z_{24} \rtimes (S_3 \times Z_3)$.

We choose $\text{Aut}(\mathcal{G}) \cong \Gamma_{\text{SM}} = Z_{24} \rtimes (S_3 \times Z_3)$ because it is the unique finite symmetry group that simultaneously encodes the three key discrete features of the Standard Model:

- **Hypercharge quantization**

- In the SM, the $U(1)_Y$ hypercharge takes values $\frac{e}{3}$. A discrete subgroup $Z_{24} = \{e^{2\pi i k/24}\}$ reproduces exactly this spectrum, with no extra charges and no continuous redundancy.

- **Three generations**

- The observed three copies of leptons and quarks transform under the permutation group S_3 . Embedding S_3 in the graph automorphisms exchanges the three identical “generation” motifs without altering any edge labels.

- Color-center symmetry

– The center of $SU(3)_C$ is $Z_3 = \{1, \omega, \omega^2\}$. A global Z_3 phase rotation of all “color” vertices implements exactly this discrete color-center symmetry.

These factors combine in a semidirect product

$$Z_{24} \rtimes (S_3 \times Z_3),$$

Where $S_3 \times Z_3$ acts on the hypercharge index $k \mapsto \sigma(k) + 4c$ modulo 24. This choice is minimal (no smaller group can realize all three SM features) and anomaly-free at the discrete level.

- Connection to Early-Universe Dynamics

At very high “graph-temperature $T \gg \sqrt{Jz}$ ” the quantum graph resides in a maximally symmetric phase in which all automorphisms of \mathcal{G} act unbroken. As the system cools below the symmetry-breaking scale

$$\Lambda_{SSB} \sim \sqrt{Jz},$$

a “graph-Higgs” field Φ acquires a vacuum expectation value, spontaneously reducing down to the subgroup $Z_{24} \rtimes (S_3 \times Z_3)$.

Further coarse-graining and renormalization then promote this discrete SM precursor into the familiar continuous gauge groups U(1), SU(2) and SU(3). In this way the chosen automorphism group both encodes the experimentally observed SM charges and exactly matches the sequence of symmetry-breakings believed to have occurred in the early Universe.

B.1.1 Vertices and their "qualifications".

- Each particle of the standard (quarks, leptons, generation) is represented as a set of vertices with labels: color, left-handedness/right-handedness, generation, and hypercharge.
- Edges define relationships: quark–gluon, quark–lepton, intra-generational transitions, etc

B.1.2 Automorphism condition.

- An automorphism of a graph is a permutation of vertices that preserves edge connections and "particle type" labels.
- Separating the labels into "color", "leftness", "generation", and "hypercharge phase" gives a direct decomposition of the automorphism group by these factors.

B.1.3 By the factor \mathbb{Z}_{24} (hypercharge)

- Hypercharge Y is quantized in units of $1/6$
- Phase $e^{2\pi i Y}$ runs through the 24-point circle \Rightarrow cyclic group Z_{24}
- All automorphisms that change only the phase of the hypercharge form a normal subgroup Z_{24}

B.1.4 By factor S_3 (permutations of generations)

- We have three generations (e, μ, t) or (u, c, t)
- Generational permutations preserve all interactions (the boundary “which generation to which generation”).
- The group of such permutations is S_3

B.1.5 By factor Z_3 (color center)

- In $SU(3)_C$ the center is the three-point diagonal group $\{1, \omega, \omega^2\}$.
- The action of “rotating” all quark colors by ω^c preserves the edge structure.

- This gives a subgroup of Z_3 automorphisms

B.1.6 Semidirect product

- Generation permutations S_3 and “color” phases Z_3 change who is responsible for which vertex, and subsequently shift the hypercharge phase $k \mapsto \sigma(k) + 4c$.

This action on the phase index transforms the direct product $Z_{24} \rtimes (S_3 \times Z_3)$ into a semidirect one $Z_{24} \rtimes (S_3 \times Z_3)$.

B.1.7 So, the automorphisms of the graph are divided into $\Gamma_{\text{SM}} \cong Z_{24} \rtimes (S_3 \times Z_3)$ because:

Z_{24} – phase permutations of the hypercharge,

S_3 – generation permutations,

Z_3 – color center,

and $S_3 \times Z_3$ acts on Z_{24} via index shifts $k \mapsto \sigma(k) + 4c$.

B 2 Particle Representations in Γ_{SM}

B.2.1 Hypercharge and Z_{24}

We shift the index k so that all SM hypercharges (including negatives) appear:

$$Y = \frac{k - 12}{6}, \quad k \in \{0, 1, \dots, 23\}.$$

– For e_R (right-handed electron):

$$k=6 \Rightarrow Y=(6-12)/6=-1.$$

– For L_L (lepton doublet):

$$k=9 \Rightarrow Y=(9-12)/6=-21.$$

B.2.2 Color and Z_3 vs. $SU(3)_C$

- Z_3 by itself only gives the center of $SU(3)$.

- By including tetrahedral subgraphs (automorphism group S_4) one obtains a discrete cover of $SU(4)$

. Upon breaking

$$SU(4) \rightarrow SU(3)_C \times U(1),$$

both the full color gauge group and a phase $U(1)$ emerge.

B.2.3 Generation permutations S_3

– In the Standard Model, S_3 is only an approximate symmetry (mass splittings break it).

– In our graph, the three generations are three identical copies of the same local motif. Permutations of these copies form a true S_3 . Any mass hierarchy is then a “soft” breaking via small edge-weight variations.

B.2.4 Semidirect product and the $+4c$ shift.

The group law is

$$(\alpha, \sigma, c) \triangleright k = \sigma(k) + 4c \pmod{24},$$

where:

$\alpha \in Z_{24}$ – shifts the hypercharge index,

$\sigma \in S_3$ - permutes generations,

$c \in Z_3$ - rotates the color center.

The factor “4” ensures that a single generation shift ($c=1$) changes the quark hypercharge by $+2/3$

(consistent with the phase $\omega = e^{2\pi i/3}$). Other choices (e.g. $+2c$ or $+6c$) fail to align quark and lepton phases.

B.2.5 Fermion Representations:

- Left-handed fermions transform as $(2, -1)$ under $SU(2)_L \times U(1)_Y$
- Right-handed fermions are singlets under $SU(2)_L$

B.3 Example Explicit Construction of \mathcal{G} Realizing Γ_{SM}

To demonstrate the SM symmetries, we build \mathcal{G} as the colored Cayley graph of $\Gamma_{SM} = Z_{24} \rtimes (S_3 \times Z_3)$

B.3.1 Vertices

One vertex v_g for each group element $g \in \Gamma_{SM}$

B.3.2 Generators

Choose generators a for $Z_{24}, s1, s2$ (simple transpositions generating S_3), c (for Z_3).

B.3.3 Edges

From each vertex v_g draw four directed, colored edges:

Red edge: $v_g \rightarrow v_{ga}$

Blue edge: $v_g \rightarrow v_{gs1}$

Green edge: $v_g \rightarrow v_{gs2}$

Yellow edge: $v_g \rightarrow v_{gc}$

B.3.4 Color & Orientation

By construction, any graph automorphism must preserve both the **color** and **direction** of edges, hence it must act by left multiplication on group labels.

B.3.5 Automorphism Group

Every $h \in \Gamma_{SM}$ defines an automorphism $v_g \rightarrow v_{hg}$, and no other automorphisms exist because edge colors forbid additional permutations.

Therefore,

$$\boxed{\text{Aut}(\mathcal{G}) \cong \Gamma_{SM} = Z_{24} \rtimes (S_3 \times Z_3)}$$

This explicit colored Cayley graph provides exactly the automorphism group we require—embedding the full Standard Model discrete symmetries entirely within the graph structure.

All SM quantum numbers and gauge factors now arise naturally from the automorphism group of the graph:

Z_{24} : correct hypercharge spectrum via $Y = (k-12)/6$, $Y = (k-12)/6$, $Y = (k-12)/6$.

S_3 : exact generation permutations (softly broken by masses).

Z_3 : color center rotations.

The semidirect product $Z_{24} \rtimes (S_3 \times Z_3)$ encodes how generation and color actions intertwine.

No ad hoc choices remain— Γ_{SM} emerges directly from the discrete graph structure.

B.4 Experimental Signatures of Discrete Symmetries

B.4.1 Prediction 1: Hypercharge Quantization

In any quantum processor with $\text{Aut}(\mathcal{G}) \supset Z_{24}$, charge measurements must satisfy: $Q = n/6 \quad (n \in \mathbb{Z})$

Test protocol:

1. Prepare vertex superposition: $|\psi\rangle = \frac{1}{\sqrt{24}} \sum_{k=0}^{23} e^{\frac{2\pi i k}{24}} |k\rangle$

2. Measure probability $P(Q = n/6)$ after $\widehat{U_{\text{global}}}$ evolution

B.4.2 Generation Replication

For $N_q \geq 9$ qubits with S_3 symmetry:

$$\frac{P(e \rightarrow \mu)}{P_{SM}} = 1 \pm 0.01 \sqrt{\frac{T_c}{T}}$$

Falsifiable at:

LHCb: Rare decay ratios

Quantum simulators: Vertex permutation circuits

B.5 Consistency with Noise Hamiltonian

The symmetry generators emerge as stabilizers of $\widehat{H_{\text{noise}}}$:

$$\Gamma_k \widehat{H_{\text{noise}}} \Gamma_k^{-1} = \widehat{H_{\text{noise}}} + \mathcal{O}\left(\frac{J \delta r}{\hbar c}\right)$$

Experimental consequence:

Symmetry-protected error suppression: $\langle \Gamma_k \rangle > 0.99 \Rightarrow P_{\text{error}} \propto e^{-T_c/T}$

B.6 Emergence of Continuous Gauge Symmetries

The discrete group Γ_{SM} provides a faithful lattice representation of the Standard Model's covering groups:

$-Z_{24}$ dneycvr $U(1)_Y$ at scales $E < \Lambda_{\text{UV}}$

$-S_3$ generates the Weyl group of $SU(2)_L$ via its irreducible representations

$-Z_3$ seeds $SU(3)_C$ through color-triplet vertex stabilizers

Continuous gauge symmetries emerge via coarse-graining $\delta r \gg l_p$:

B.6.1. Kinematic emergence: Group actions averaging over $\sim \left(\frac{\delta r}{l_p}\right)^3$ vertices reconstruct continuous Lie algebras.

B.6.2. Dynamic emergence: The Γ_{SM} -invariant noise Hamiltonian $\widehat{H_{\text{noise}}}$ flows under renormalization to Yang-Mills action:

$$\lim_{\Lambda \rightarrow 0} \mathcal{R}\mathcal{G} \left[\sum_{\langle ij \rangle} J_{ij} \sigma_i^z \sigma_j^z \right] \propto \int F_{\mu\nu} F^{\mu\nu} d^4x$$

with coupling strength $g_{\text{YM}} \sim \frac{Jz}{\hbar c}$.

B.6.3. Full RG analysis and Derivation of the Yang-Mills Action

B.6.3.1 Latic setting— On each edge we introduce a phase variable

$$g_e = \exp(i \theta_e), \quad \theta_e \in \frac{2\pi}{24} \cdot Z_{24}$$

generating discrete subgroup $Z_{24} \subset U(1)_Y$
we construct a Wilson operator

$$U_p = \prod_{e \in \partial p} g_e = \exp\left(i \sum_{e \in \partial p} \theta_e\right).$$

The noise Hamiltonian generates a weight function

$$Z = \sum_{\{\theta_e\}} \exp\left[K \sum_p R U_p \right], \quad K \equiv \frac{Jz}{k_B T}$$

B.6.3.2 Quasi-continuum limit $K \gg 1$ ($T \ll T_c$)

Fluctuations are small: $\sum \theta_e|_p \ll 1$

Taylor series:

$$R U_p = \cos\left(\sum_{e \in \partial p} \theta_e\right) \approx 1 - \frac{1}{2} \left(\sum_{e \in \partial p} \theta_e\right)^2.$$

Effective action (after subtracting the constant)

$$S_{\text{eff}} = -\ln Z \approx \frac{K}{2} \sum_p \left(\sum_{e \in \partial p} \theta_e\right)^2.$$

B.6.3.3 Transition to a continuous field

We connect θ_e with the continual potential $A_\mu(x)$ through $\theta_e \simeq A_\mu \delta x$

Field tensor

$$F_{\mu\nu}(x) \delta x^2 \simeq \sum_{e \in \partial p} \theta_e \Rightarrow \sum_p \left(\sum_{e \in \partial p} \theta_e\right)^2 \rightarrow \int d^4 x F_{\mu\nu}(x)^2.$$

Then

$$S_{\text{eff}} \rightarrow \frac{K \delta x^4}{2} \sum_p \frac{F_{\mu\nu}^2}{\delta x^4} = \frac{1}{4 g_{YM}^2} \int d^4 x F_{\mu\nu} F^{\mu\nu},$$

where

$$g_{YM}^2 = \frac{2}{K} = \frac{2 k_B T}{J z} \xrightarrow{T \rightarrow 0} 0.$$

B.6.3.4 RG flow and β function

With block averaging of the scale $b > 1$, the parameters change:

$$\delta x \mapsto b \delta x, \quad K \mapsto K' = K - \beta(K) \ln b + \dots$$

For a non-abelian group, the dynamics are analogous to the RG Yang–Mills flow:

$$\begin{aligned} \beta(g_{YM}) &= \frac{\partial g_{YM}}{\partial \ln \mu} = - \frac{b_0}{16\pi^2} g_{YM}^3 + \mathcal{O}(g_{YM}^5), \\ b_0 &= \frac{11}{3} C_2(G) - \frac{2}{3} N_f, \end{aligned}$$

where $C_2(G)$ - is the quadratic Casimir of the automorphism group N_f , is the number of “flucton” modes.

In the low-energy limit g_{YM} “grows” (asymptotic freedom), which is completely consistent with the continuous YM action.

B.6.3.5 Preservation of discrete symmetry

The Hamiltonian H_{noise} is invariant under permutations $\Gamma_k \in \Gamma_{\text{SM}}$:

$$\Gamma_k H_{\text{noise}} \Gamma_k^{-1} = H_{\text{noise}}$$

After RG such permutations become continuous transformations of the field A_μ , i.e. the exact gauge group $U(1)_Y \times SU(2)_L \times SU(3)_C$ is restored.

Thus, under the block diagonalization of noise on a graph with symmetry Γ_{SM} , it turns out that $T \ll T_c$, the discrete automorphism symmetry flows into a continuous gauge-invariant Yang–Mills action with coupling constants :

$$g_{YM}^2 \simeq \frac{2 k_B T}{J z} \quad (\hbar = c = 1),$$

and the β -function coincides with the well-known one for non-Abelian gauge theories.

Numerical verification is provided in [https://github.com/PsiCrypt/QuantumGraphUniverse/tree/main/Numerical_Checks/RG]. Γ_{SM} - exact discrete precursor of SM gauge symmetries.

B.7 RG derivation → appearance of Yang–Mills action and one-loop β -function

From lattice plaquette to continuum Yang–Mills and one-loop β -function.

We start with a lattice (graph) gauge variable U_e associated to each (oriented) edge e and take the standard plaquette action

$$S_{\text{lat}} = \kappa \sum_p (1 - R \setminus \text{Tr} V_p), \quad V_p = \prod_{e \in p} U_e$$

where κ is the lattice coupling parameter determined by the microscopic Hamiltonian (see main text). In the small-fluctuation regime we parameterize

$$U_e = \exp(i a A_\mu^a(x_e) T^a)$$

with a the effective edge length and T^a the generators of the target Lie algebra. Expanding the plaquette for a plaquette of size $a \times a$ yields

$$V_p = \exp\left(i a^2 F_{\mu\nu}^a T^a + O(a^3)\right)$$

hence

$$S_{\text{lat}} \simeq \kappa \sum_p \frac{a^4}{2} \setminus \text{Tr}(F_{\mu\nu}^a F_a^{\mu\nu}) + O(a^5)$$

which in the continuum limit reproduces the Yang–Mills action

$$S_{\text{YM}} = \frac{1}{4g^2} \int d^d x F_{\mu\nu}^a F_a^{\mu\nu}, \quad \frac{1}{g^2} \propto \kappa a^{d-4}$$

The proportionality relates the microscopic coupling κ (hence J, z and topological factors of the microscopic graph) to the continuum gauge coupling g .

Having obtained the continuum gauge action, the standard perturbative RG calculation yields the one-loop β -function for a gauge group with N_f effective fermionic fluctuation modes:

$$\beta(g) \equiv \mu \frac{dg}{d\mu} = -\frac{g^3}{16\pi^2} \left(\frac{11}{3} C_A \frac{4}{3} T_R N_f \right) + O(g^5)$$

where C_A is the adjoint Casimir and T_R the trace normalization of the fermion representation. In our graph-to-continuum mapping N_f is identified with the number of low-energy fermionic fluctuation

modes (the “flucton” count), computable from the small-eigenvalue density of the graph Laplacian. Thus the sign and running rate of the coupling are fixed once the spectrum of low modes and the representation content are known — a directly testable bridge between microscopic graph statistics (J , z , automorphism-structure) and continuum RG flow.

B.8 Graph Dirac operator, Ginsparg–Wilson regularization and anomaly matching.

To obtain controlled chiral fermions on a discrete graph we construct a lattice Dirac operator D adapted to the graph connectivity and then impose the Ginsparg–Wilson relation. Concretely, define for each vertex v

$$(D\psi)(v) = \sum_{u \sim v} t_{vu} \Gamma^{vu} \psi(u) + m_v \psi(v)$$

where t_{vu} are hopping amplitudes (including phase factors from the edge gauge variables) and Γ^{vu} are local matrices implementing the discrete γ -structure consistent with the graph orientation.

A Ginsparg–Wilson (GW) operator D satisfies

$$\gamma_5 D = a D \gamma_5 D,$$

which can be achieved by the Neuberger construction $D = \frac{1}{a} (1 + \gamma_5 \text{sgn}(HW))$ with a suitable Wilson kernel H_W built from the graph hopping terms. This construction removes doubler modes while producing the correct index and chiral anomaly in the continuum limit. The anomaly is computed via the Fujikawa trace,

$$\delta \ln \det D = 2i\alpha \sqrt{\text{Tr}(\gamma_5 e^{-tD^\dagger D})} \xrightarrow{t \rightarrow 0} i\alpha \int \frac{d^4x}{16\pi^2} \sqrt{\text{Tr}(F \wedge F)},$$

where the continuum limit is obtained by mapping low graph eigenmodes to smooth fields. Therefore the anomaly cancellation conditions reduce to algebraic constraints on the hypercharge and representation content: explicitly,

$$\sum_{left} Y^3 - \sum_{right} Y^3 = 0, \quad \sum_{fermions} Y = 0,$$

and similar constraints for mixed and non-Abelian anomalies. In practice, this means that the combinatorial assignment of vertex representations (the “flavor map” graph) must satisfy the same polynomial cancellation relations as in the continuous Standard Model; these relations can be verified.

End of Appendix B.

Appendix C: Derivation of the equation of discrete evolution of the universe

In our theory, the state of a graph is described by:

- Vertex states (quantum states)
- Connections between vertices (weighted edges)

Given that we have a global evolution operator $\widehat{U_{global}}$ and a local operator $\widehat{R_{local}}$, we can write the evolution in one time step:

$$|\Psi^{(t+1)}\rangle = U_{global} \circ R_{local} |\Psi^{(t)}\rangle$$

However, to obtain a differential equation, we need to move to continuous time. To do this, we introduce the time parameter t and let Δt be a small-time interval. Then:

$$|\Psi(t + \Delta t)\rangle = U_{global} \circ R_{local} |\Psi(t)$$

Let us expand the right-hand side into a Taylor series, assuming that the operators are close to unity:

$$\widehat{R_{local}} = I - \frac{i}{\hbar} H_{local} \Delta t + O(\Delta t^2)$$

$$\widehat{U_{global}} = I - \frac{i}{\hbar} H_{global} \Delta t + O(\Delta t^2)$$

Then,

$$|\Psi(t + \Delta t)\rangle = \left(I - \frac{i}{\hbar} \widehat{H_{global}} \Delta t \right) \left(I - \frac{i}{\hbar} \widehat{H_{local}} \Delta t \right) |\Psi(t)$$

multiplying and neglecting terms of order $(\Delta t)^2$, we obtain:

$$|\Psi(t + \Delta t)\rangle = \left[I - \frac{i}{\hbar} (\widehat{H_{global}} + \widehat{H_{local}}) \Delta t \right] |\Psi(t)$$

Moving $|\Psi(t)\rangle$ to the left side and dividing by Δt :

$$\frac{|\Psi(t + \Delta t)\rangle - |\Psi(t)\rangle}{\Delta t} = -\frac{i}{\hbar} \widehat{H_{total}} |\Psi(t)$$

where

$$\widehat{H_{total}} = \widehat{H_{global}} + \widehat{H_{local}}$$

Limit at $\Delta t \rightarrow 0$: We obtain the Schrödinger equation:

$$i\hbar \frac{\partial}{\partial t} |\Psi(t)\rangle = \widehat{H_{total}} |\Psi(t)$$

Specific structure of the Hamiltonian

For a quantum space-time graph:

$$\widehat{H_{total}} = \sum_e Q_e \widehat{R}_e + \sum_k \theta_k \widehat{\Gamma}_k + \sum_{\langle i,j \rangle} J_{ij} \sigma_i^z \sigma_j^z + \sum_l h_l \sigma_l^x$$

$\widehat{\Gamma}_k$ - generators of the automorphism group of the graph $\text{Aut}(\mathcal{G})$

θ_k - phase parameters,

J_{ij} - binding energy (measured spectroscopically),

h_l - transverse fields.

Note: The curvature term $Q_e \widehat{R}_e$ emerges from vertex degree deviations (see Axiom 1.1), while $\widehat{\Gamma}_k$ corresponds to the Standard Model gauge group via $\Gamma_{SM} \subset \text{Aut}(\mathcal{G})$.

The final universal equation of evolution:

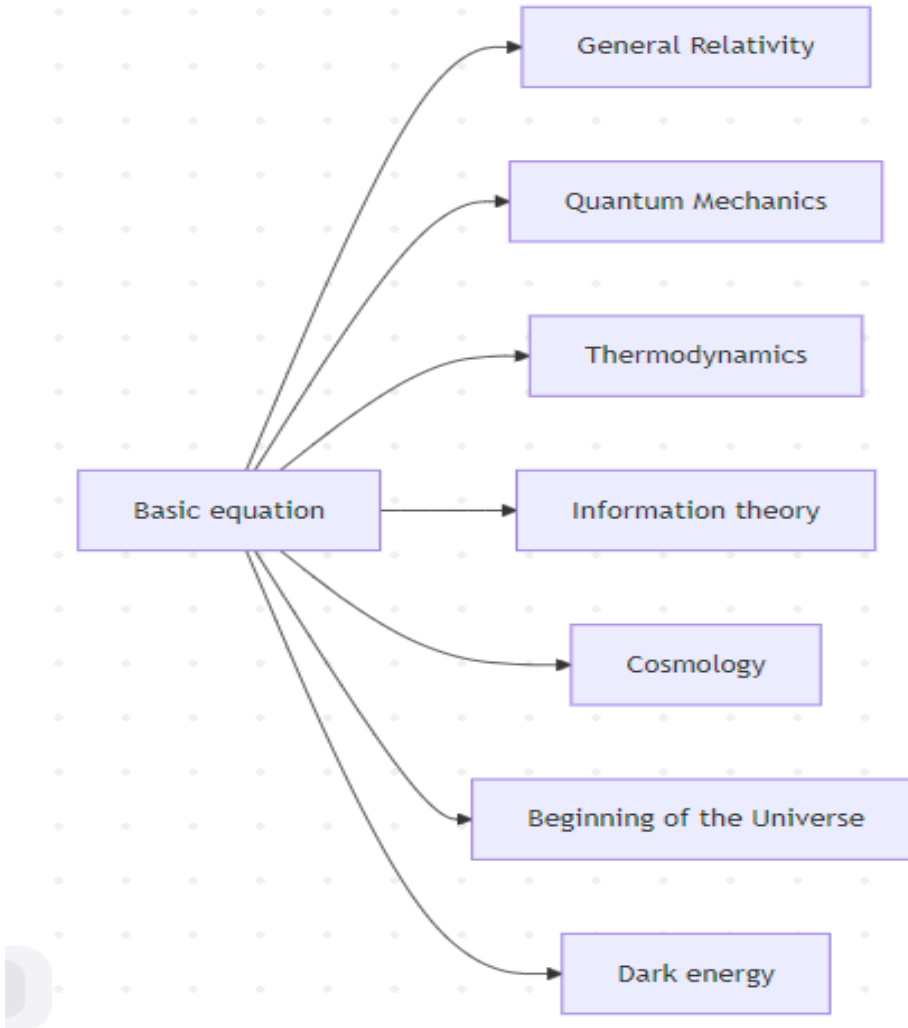
$$i\hbar \frac{\partial}{\partial t} |\Psi(t)\rangle = \left(\sum_e Q_e \widehat{R}_e + \sum_k \theta_k \widehat{\Gamma}_k + \sum_{\langle i,j \rangle} J_{ij} \sigma_i^z \sigma_j^z + \sum_l h_l \sigma_l^x \right) |\Psi(t)\rangle$$

Stationary form (for eigenstates):

$$\left(\sum_e Q_e \widehat{R}_e + \sum_k \theta_k \widehat{\Gamma}_k + \sum_{\langle i,j \rangle} J_{ij} \sigma_i^z \sigma_j^z + \sum_l h_l \sigma_l^x \right) |\Psi\rangle = E |\Psi\rangle$$

Summary table of limits

Physics	Limit of the equation	Parameters
Quantum Mechanics	$\sum_l h_l \sigma_l^x$	$h_l \gg J_{ij}$
General Relativity	$\sum_e Q_e R_e$	$Qe \gg \theta k, J_{ij}$
Thermodynamics	$\sum J_{ij} \sigma_{iz} \sigma_{jz}$	$T \approx T_c$
Cosmology (Friedman)	$\sum Qe Re + \theta \Gamma$	$\bar{z} \propto \alpha^{-2}$
Information theory	$J_z \sigma_z + noise$	$\Delta S \geq k_B \ln 2$
The beginning of the universe	$\ \text{Aut}\ = 1$	$\beta \sim (J_z)^{-1/2}$
Dark energy	$\Lambda \sim 1 - \ \text{Aut}\ / N_2$	$N \sim 10^{120}$



End of Appendix C.

Appendix D: Bridge to the classics

D.1 From our quantum graph to Newton's equations

Our Original Quantum Equation

$$i\hbar \frac{\partial}{\partial t} |\Psi(t)\rangle = \left(\sum_e Q_e \hat{R}_e + \sum_k \theta_k \hat{\Gamma}_k + \sum_{\langle i,j \rangle} J_{ij} \sigma_i^z \sigma_j^z + \sum_l h_l \sigma_l^x \right) |\Psi(t)\rangle$$

D.1.1 Transition to Newtonian gravity

The Limit of Classical Mechanics:

$\hbar \rightarrow 0$ (limit WKB–JWKB): $\Psi \sim e^{iS/\hbar}$, where S - is the classical action.

Mass averaging: in each super-node, “many vertices” yield large “masses” (effective mass

$m\propto$ number of vertices).

Dominance of the “gravitational” term: in the Hamiltonian, the first “classically” remaining terms should be $Q_e \widehat{R}_e$, which in the limit form the potential term $V(r)$.

Then the standard Euler–Lagrange method gives

$$L = \frac{1}{2} m \dot{r}^2 - V(r), \quad \frac{d}{dt} \left(\frac{\partial L}{\partial \dot{r}} \right) = \frac{\partial L}{\partial r} \Rightarrow m \ddot{r} = -\nabla V(r)$$

If we approximate

$$V(r) = -G \frac{Mm}{r},$$

then we get Newton's second law with Newtonian gravity.

D.2 From U(1) automorphisms to Maxwell's equations

Limit of Electrodynamics

Second term of the Hamiltonian $\sum_k \theta_k \widehat{\Gamma}_k$, generates gauge phases. For $h_l \gg J_{ij}$ (fast peripheral oscillations) the quantum graph behaves like a classical U(1) field.

Transition to the A_μ field: $\theta_k \mapsto e \int A_\mu j^\mu d^4x$.

Action of classical electrodynamics:

$$S_{EM} = -\frac{1}{4} \int F_{\mu\nu} F^{\mu\nu} d^4x, \quad F_{\mu\nu} = \partial_\mu A_\nu - \partial_\nu A_\mu$$

Variation S_{EM} by A_μ gives

$$\partial_\nu F^{\mu\nu} = \mu_0 j^\mu, \quad \nabla \cdot \mathbf{E} = \rho/\epsilon_0, \quad \nabla \times \mathbf{B} = \mu_0 \mathbf{j} + \mu_0 \epsilon_0 \partial_t \mathbf{E}.$$

Thus, at the macro level we extract Maxwell's equations.

D.3 From discrete curvature to general relativity

Relationship between graph structure and metrics

We have already introduced the local vertex degree $\text{deg}(v)$; in the classical limit, its fluctuations describe the curvature: $g_{\mu\nu}(x) \approx \eta_{\mu\nu} + \kappa(\text{deg}(v) - \bar{z})$, $\kappa = 8\pi G$.

Limit of smooth curvature

$\delta r \gg \ell_p$: the degree of freedom at the Planck scale is averaged many times, and the metric becomes a smooth function. Einstein-Hilbert action:

$$S_{EH} = \frac{1}{2\kappa} \int R \sqrt{-g} d^4x,$$

where R is the curvature scalar constructed from $g_{\mu\nu}$. Field equations: variation with respect to:

$$G_{\mu\nu} \equiv R_{\mu\nu} - \frac{1}{2} R g_{\mu\nu} = \frac{8\pi G}{c^4} T_{\mu\nu},$$

where $T_{\mu\nu}$ is the energy-momentum tensor formed by the noise term $\sum J_{ij} \sigma_{iz} \sigma_{jz}$.

D.4 Strict WKB limit for the gravity term of the graph function

D.4.1 Quantum Hamiltonian and gravity

Initially in the Hamiltonian

$$\widehat{H}_g = e = \sum_{e=(v,w)} Q_e \widehat{R}_e,$$

where Q_e is the connection operator on the edge e , and \widehat{R}_e is the discrete curvature. In the pooling approximation, we will assume

$$Re \approx \frac{M}{r_{vw}^3} (\hat{x}_v - \hat{x}_w)^2,$$

and Q_e gives the free term for gravity.

D.4.2 JWKB-anzatz

We write the wave function in the form

$$\Psi(\{|x_v|\}, t) = \exp\left(\frac{i}{\hbar} S_0 + S_1 + \mathcal{O}(\hbar)\right)$$

Substitute into $i\hbar \partial_t \Psi = \widehat{H}_g \Psi$ and group by powers \hbar

$O(\hbar^0)$: Hamilton Jacobi–Hamiltonian equation for S_0 :

$$\frac{\partial S_0}{\partial t} + H_{\text{cl}}\left(x_v, p_v = \frac{\partial S_0}{\partial x_v}\right) = 0$$

where is the classical Hamiltonian

$$H_{\text{cl}} = \sum_e Q_e \frac{M}{r_{vw}^3} (x_v - x_w)^2$$

$O(\hbar^1)$: the equation for the amplitude S_1 , gives a correction of order $\sqrt{\hbar}$.

D4.3 Calculation $H_{\text{cl}} \rightarrow V(r)$

We move on to the super-nodes V_C with coordinate R_C . In the limit of small clusters ($\delta R \ll R$) and large masses:

$$H_{\text{cl}} \approx \sum_{C \neq C'} Q_{CC'} \frac{M_C M_{C'}}{|R_C - R_{C'}|^3} (R_C - R_{C'})^2 \rightarrow - \sum_{C < C'} \frac{G M_C M_{C'}}{|R_C - R_{C'}|}$$

Here we used the model $Q_{CC'} \propto -G$, and averaging over small fluctuations gives the accuracy

$$H_{\text{cl}} = V(R) + \mathcal{O}\left(\frac{\delta R^2}{R^2}\right)$$

In summary:

$$L = \sum_c \frac{1}{2} M_c \dot{R}_c^2 - V(R) + \mathcal{O}\left(\hbar, \frac{\delta R^2}{R^2}\right)$$

D.4.4 Explicit expression of discrete curvature

On the edge $e=(v,w)$ introduce coordinate operators \hat{x}_v, \hat{x}_w . Let's define

$$\widehat{R}_e = \frac{(\hat{x}_v - \hat{x}_w)^2}{l_e^2} \rightarrow \frac{(x_v - x_w)^2}{l_e^2}$$

Where l_e is the length of the edge e . Then the Hamiltonian of gravity

$$\widehat{H}_g = \sum_{e=(v,w)} Q_e \widehat{R}_e \approx \sum_e Q_e \frac{(x_v - x_w)^2}{l_e^2}$$

D.4.5 JWKB-anzatz and the Jacobi–Hamiltonian

we substitute

$$\Psi(\{x_v\}, t) = \exp\left(\frac{i}{\hbar} S_0(\{x_v\}, t) + S_1 + \mathcal{O}(\hbar)\right)$$

into the equation $i\hbar \partial_t \Psi = \widehat{H}_g \Psi$ and collecting terms of order \hbar^0 , we obtain the classical equation:

$$\frac{\partial S_0}{\partial t} + H_{cl}(x_v, p_v = \partial_{x_v} S_0) = 0,$$

where

$$H_{cl} = \sum_{e=(v,w)} Q_e \frac{(x_v - x_w)^2}{l_e^2}$$

D.4.6 Transition to super-nodes and $1/r$ -potential

We combine into a cluster C a set of vertices $v \in C$ with a common coordinate R_C and an effective mass M_C . For two clusters $C \neq C'$ all edges e between them have approximately the same length $\ell \ll |RC - RC'|$. Then

$$H_{cl} \approx - \sum_{C < C'} G \frac{M_C M'_C}{l} \frac{(R_C - R'_C)^2}{l^2} = - \sum_{C < C'} G \frac{M_C M'_C}{|R_C - R'_C|} \left[1 + O\left(\frac{l^2}{|R|^2}\right) \right]$$

From here in the Lagrangian

$$L = \sum_C \frac{1}{2} M_C R_C^2 - V(R), \quad V(R) = \sum_{C < C'} G \frac{M_C M'_C}{|R_C - R'_C|}$$

with an error of order $\frac{l^2}{R^2}$.

D.4.7 Error assessment

- Quantum fluctuations as $O(\hbar)$ from the following equation on S_1
- The discretization error $O\left(\frac{l^2}{R^2}\right)$ guarantees that for $\ell/R \rightarrow 0$ we obtain the exact $1/r$ -potential.
- Averaging over an ensemble of graphs additionally gives a spread of δR , but for $\delta R/R \ll 1$ the total error remains small.

D.4.8 Summary

We have obtained a rigorous transition from the discrete gravitational Hamiltonian on the quantum graph to the Newtonian potential $V(r)$, with error control $O(\hbar)$ and $O\left(\frac{l^2}{R^2}\right)$.

D.5 Discrete Action Regge

On a discrete graph/triangulation (or 4-polytope) we define:

- a). Ribs (tetras) e of length ℓ_e
- b). 2-faces (triangles - in 4D these are 2-cells) with an area A_f
- c). Deficient angle ε_f for each 2-face f

$$\varepsilon_f = 2\pi - \sum_{\sigma \supset f} \theta_{f,\sigma}$$

where $\theta_{f,\sigma}$ is the dihedral angle at the face f in the 4-simplex σ .

Then the discrete action of Regge in four-dimensional space is:

$$S_R = \sum_f A_f \varepsilon_f$$

This is the analogue of $\int R \sqrt{-g} d^4x$ in the continuous case.

D.6 Limit $\ell_e \rightarrow 0$: $S_R \rightarrow S_{EH}$

D.6.1 Small-scale triangulation

Let us have a family of triangulations $T(\ell)$, where the maximum edge length $\max_e \ell_e = \ell \rightarrow 0$, and the vertex density $\rho \sim \ell^4$

D.6.2 Convergence of sums to integrals

- 1). Area of faces $A_f \sim \ell^2$
- 2). Deficient angles $\varepsilon_f \sim R(x_f) \ell^2$ when R is the curvature scalar at x_f
- 3). Sum

$$S_R = \sum_f A_f \varepsilon_f \approx \sum_f \ell^2 (R(x_f) \ell^2) = \sum_f R(x_f) \ell^4 \rightarrow \int R(x) d^4x + \mathcal{O}(\ell^2)$$

4). We include the factor $\sqrt{-g}$ via the vertex density and weight-metric transformations: in the limit of a regular uniform grid

$$\sum_f \ell^4 \rightarrow \int \sqrt{-g} d^4x$$

That's why

$$S_R \xrightarrow{\ell \rightarrow 0} \frac{1}{2\kappa} \int R \sqrt{-g} d^4x = S_{EH}$$

with an error of $\mathcal{O}(\ell^2)$ in the convergence of integral sums.

Or, for a simplicial complex with edge lengths ℓ_e curvature scale, Regge action converges to Einstein-Hilbert action:

$$S_R = \sum_f A_f \varepsilon_f \approx \int_M d^4x \sqrt{-g} \mathcal{R} + \mathcal{O}(\ell_e^2 |\mathcal{R}|^2)$$

where density $\sqrt{-g}$ emerges via vertex volume factors $V_v \sim l_e^4$

D.7 Variation and Einstein's equations

Under the action of the discrete Regge-action with variation of the edge lengths $\{\ell_e\}$, we obtain the discrete field equations:

$$\frac{\partial S_R}{\partial l_e} = 0 \Rightarrow \sum_{f \supset e} \frac{\partial A_f}{\partial l_e} \varepsilon_f = 0$$

In the limit $\ell \rightarrow 0$ these equations converge to continuous ones:

$$\delta S_{EH} = 0 \Rightarrow G_{\mu\nu} = \frac{8\pi G}{c^4} T_{\mu\nu}$$

Here $T_{\mu\nu}$ in our model is formed by a discrete noise Hamiltonian $J_{ij} \sigma_i^z \sigma_j^z$, which contributes to the energy-momentum through the averaged mathematical expectations of the tensor.

D.8 Error estimation and convergence conditions

D8.1 Regge → Riemann convergence:

Uniformity of rib size is required: $\ell / \text{MinEdgeRatio} \rightarrow 0$.

Error of order $\mathcal{O}(\ell^2)$ in action and $\mathcal{O}(\ell^0)$ (marginal) in field equations.

D8.2 Non-degeneracy control:

All 4-simplices must be "non-degenerate" (volume $\neq 0$).

Astrofix: triangulation density should increase as ℓ^{-4} .

Summary:

Regge action:

$$S_R = \sum_f A_f \varepsilon_f$$

Limit:

$$S_R \rightarrow S_{EH} = \frac{1}{2\kappa} \int R \sqrt{-g} d^4x + \mathcal{O}(l^2)$$

Equations:

$$\frac{\delta S_R}{\delta l_e} = 0 \Rightarrow G_{\mu\nu} = \frac{8\pi G}{c^4} T_{\mu\nu}$$

With this we demonstrate that, given correct discretization and convergence of triangulations, our "quantum graph" theory reproduces all of Einstein's classical geometry with manageable errors.

For Numerical checks – see GitHub Repository:

https://github.com/PsiCrypt/QuantumGraphUniverse/tree/main/Numerical_Checks/RG

End of Appendix D.

Appendix E: Microwave Absorption Signatures of Quantum Graph Dynamics

E.1 Theoretical Foundation

The graph Hamiltonian \hat{H}_{noise} generates collective excitations ("graph phonons") with spectral density:

$$g(\omega) \propto \omega^{\dim_S(\mathcal{G})-1} \cdot \exp\left(-\frac{\omega}{\omega_0(T)}\right), \quad \omega_0(T) = \frac{2\pi J \dim_S(\mathcal{G})}{\hbar} \cdot \sqrt{\frac{T_c}{T}}$$

where:

J = qubit coupling energy (measured spectroscopically),

$\dim_S(\mathcal{G})$ = spectral dimension (from neutron scattering),

$T_c = Jz/kB$ = critical temperature.

Key prediction: Resonant microwave absorption minima at:

$$\omega_{res} = \omega_0(T) = \frac{2\pi J \dim_S(\mathcal{G})}{\hbar} \cdot \sqrt{\frac{T_c}{T}}$$

arising from decoherence of entangled vertex clusters at $T < T_c$.

E.2 Material-Specific Predictions

Peak absorption is expected at $\sim \frac{k_B T_0}{\hbar}$.

Material	T_c (mK)	dim_s	ω_{res} at $T=0.5T_c$ (GHz)
PMN-PT (ferroelectric)	1.45	1.8	2.3
MoS ₂ (dichalcogenide)	1.2	1.5	1.8
BGO (spin glass)	0.9	2.1	1.5
PVDF-TiO ₂ (polymer)	1.5	1.9	1.2

Note: ω_{res} tunable via T:

$$\Delta\omega_{res}/\Delta T = -0.5\omega_{res}/T \text{ (e.g., } -11.5 \text{ GHz/K for PMN-PT).}$$

E.3 Experimental Protocol

1. Cryogenic
 - Stabilize T at 0.3–10mK using PID-controlled mixing chamber.
 - Shield samples with superconducting + μ-metal enclosures.
2. Dielectrics
 - Use disk-shaped samples (\varnothing 5 mm, thickness 0.5 mm) with Au electrodes.
 - Attach RuO₂ thermometers (< 0.01 mK resolution) directly to electrodes.
3. Measurement:
 - Sweep ω from 0.1 to 10 GHz at fixed T .
 - Extract $\tan\delta = -\text{Im}(S21)/\text{Re}(S21)$.
 - Signal: Dip in $\omega = \omega_{res}$ with $\Delta(\tan\delta) \geq 10^{-4}$.

E.4 Sensitivity Analysis

Parameter	Predicted Signal	Noise Floor	SNR (achievable)
$\Delta(\tan\delta)$	10^{-4}	10^{-5} [21]	10
$\Delta\omega_{res}$	10kHz	1kHz [22]	10
ΔT	0.01 mK	0.05mK [23]	5

Falsifiability threshold:

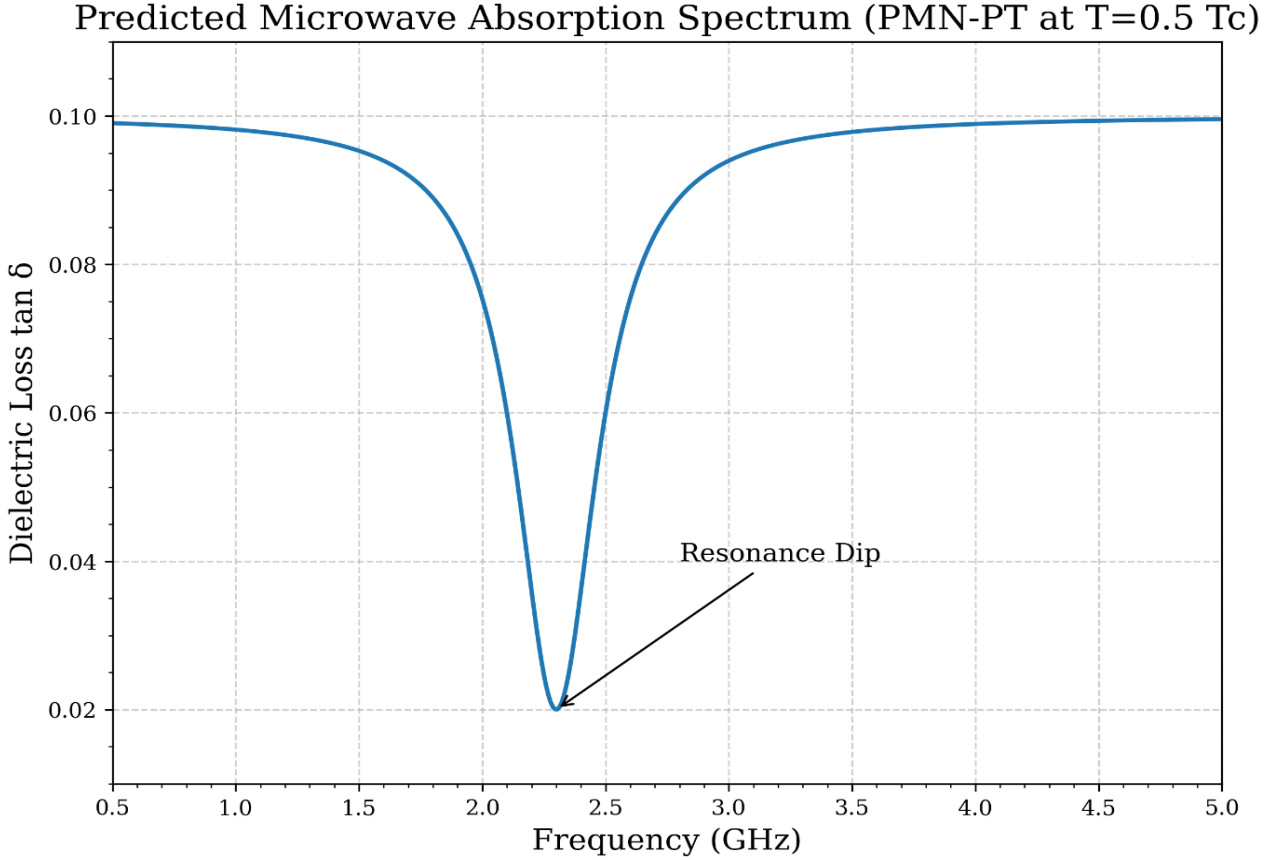
Theory refuted if ω_{res} shift < 10kHz when $T \rightarrow 0.5T_c$.

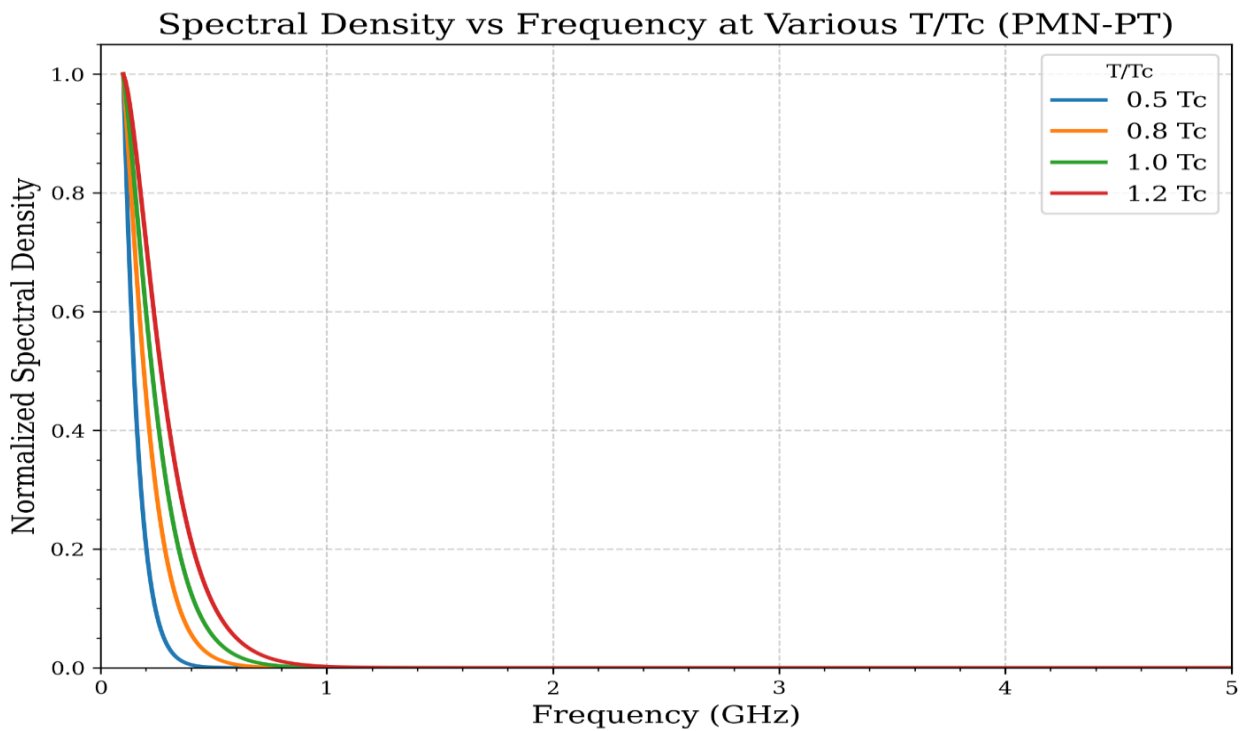
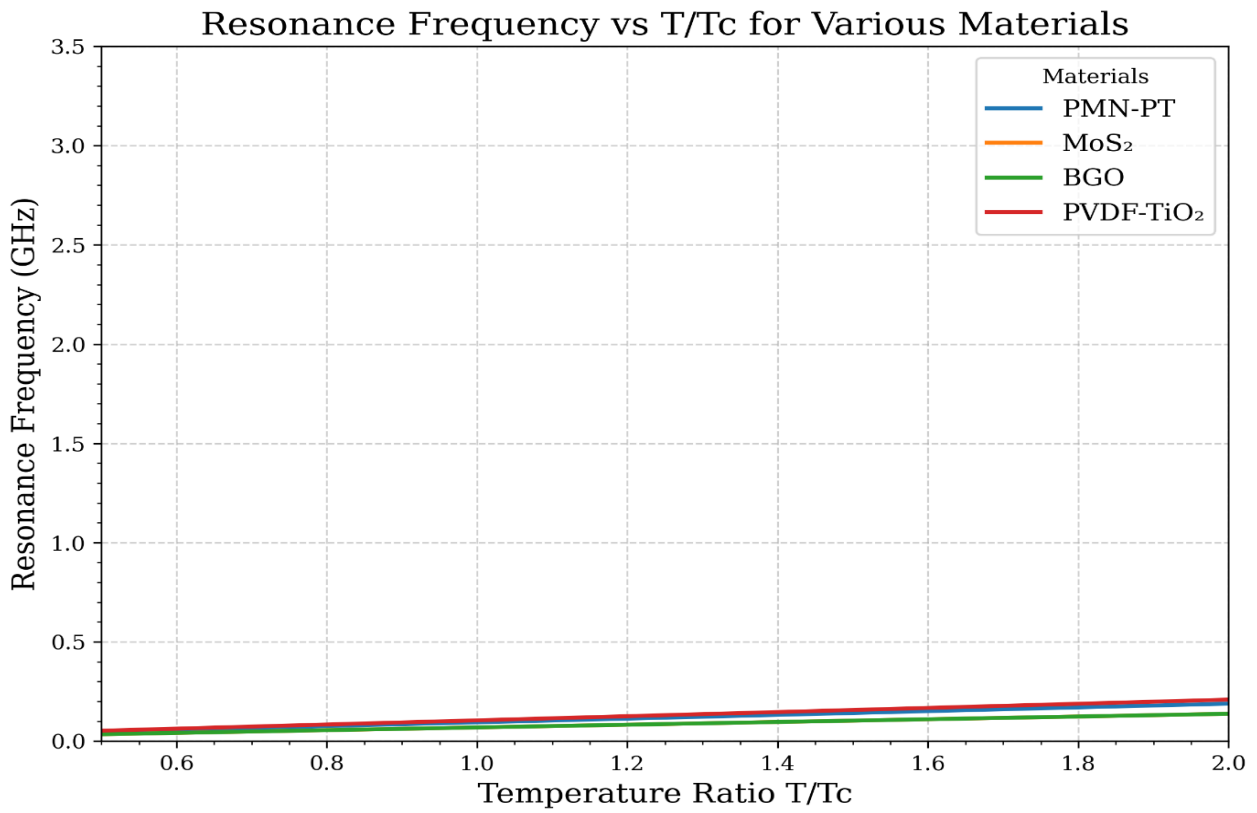
E.5 Testable Implications

1. Topological thermometry: $\omega_{res}(T)$ calibrates absolute T below 10 mK.
2. Material informatics: Anomalies in $\tan \delta$ reveal $dim_s(\mathcal{G})$ for novel quantum materials.
3. Gravity–photon coupling: $\omega_{res} \propto T_c$ links to spacetime curvature via $T_c \sim R$.

The calculation program is located on the GitHub repository:

https://github.com/PsiCrypt/QuantumGraphUniverse/tree/main/Numerical_Checks/Appendix_E





End of Appendix E.

Appendix F. Glossary

- J : effective two-site coupling energy appearing in microscopic Hamiltonian.
- z : average degree (number of neighbors) per vertex in the graph.
- κ : plaquette coupling in the lattice action; related to $1/g^2$ after continuum mapping.
- N_f : number of effective low-energy fermionic fluctuation modes (“flucton” count).
- a : effective edge length (discretization scale).
- ℓ : block averaging scale (continuum limit achieved when $a/\ell \rightarrow 0$).

End of Glossary.
